Supporting Information

A Twist in Electronic Relaxation of Pyrimidine Nucleosides and Nucleotides: Impact of C5 Methylation on Nonadiabatic Transition and Photohydration Damage

Srijon Ghosh, [1†] Yuki Obara,[1†] Vishal Kumar Jaiswal,[2†] Mario Taddei,[2†] Artur Nenov,[2] Irene Conti,*[2] Marco Garavelli*[2] and Toshinori Suzuki*[1]

[1]*Department of Chemistry, Graduate School of Science, Kyoto University, Kitashirakawa-Oiwakecho, Sakyo-Ku, 606-8502, Kyoto, Japan*

[2]*Dipartimento di Chimica industriale "Toso Montanari", Università di Bologna, via Piero Gobetti 85, Bologna 40129, Italy*

E-mail: suzuki@kuchem.kyoto-u.ac.jp, marco.garavelli@unibo.it, irene.conti@unibo.it

[†] These authors contributed equally.

A. Photoexcitation conditions

Table S1. Experimental parameters used in the present study. The solvent was phosphate buffered D_2O in all cases. The molar absorption coefficients at 267 nm were measured in H_2O.

	Units	**DUrd**	**2′-deoxy-DUrd**	**5′-deoxy-DUrd**	**DThd**	**5m-DUrd**	**DUMP**	**DTMP**	**DCMP**	**5m-DCyd**
Excitation laser wavelength	nm	267	267	267	267	267	267	267	267	267
Pulse energy	nJ	774	810	563	924	546	704	704	704	546
Focal spot size for UV pulse (FWHM)	mm	250	250	250	250	250	250	250	250	250
Probed volume	$\times 10^{-9}$ L	6.2	6.2	6.2	6.2	6.2	6.2	6.2	6.2	6.2
Concentration of nucleobase	mM	0.02	0.02	0.02	0.02	0.02	0.02	0.02	0.02	0.02
Optical path length	mm	0.005	0.005	0.005	0.005	0.005	0.005	0.005	0.005	0.005
Molar extinction coefficient	$M^{-1}\,cm^{-1}$	9690	9500	5970	8500	8410	9660	9660	7640	6090
Absorbed photons	$\times 10^{11}$ photons	2.4	2.5	1.4	2.7	1.6	2.1	2.1	2.0	1.4
Number of molecules in probed volume	$\times 10^{11}$ molecules	75	75	75	75	75	75	75	75	75
Excitation efficiency	%	3.1	3.3	1.9	3.6	2.1	2.9	2.9	2.6	1.9

B. Chemicals

Table S2. Suppliers and purities of chemicals.

Name	Supplier	Purity
Urd	FUJIFILM Wako	>98.0%
Thy	Tokyo Chemical Industry	>98.0%
Cyd	Tokyo Chemical Industry	>98.0%
5-methylCyd	Tokyo Chemical Industry	>98.0%
Urd 5′-monophosphate (disodium salt)	Tokyo Chemical Industry	>98.0%
Cyd 5′-monophosphate	Tokyo Chemical Industry	>98.0%
Thd 5′-monophosphate (disodium salt)	Combi-Blocks	>95.0%
2′-deoxyUrd	Tokyo Chemical Industry	>99.0%
5′-deoxyUrd	Amadis Chemical	>95.0%
5-methylUrd	Tokyo Chemical Industry	>98.0%
NaH_2PO_4	FUJIFILM Wako	>99.0%
Na_2HPO_4	FUJIFILM Wako	>99.0%
D_2O	FUJIFILM Wako	>99.5%

The pH values during the experiments were maintained at approximately 6.8 using 50 mM phosphate-buffered D_2O solutions. This condition ensured that the nucleobases predominantly retained their standard, biologically relevant tautomeric forms. Although variations in protonation state can potentially affect the excited-state dynamics,[1] the phosphate buffer provided sufficient stability for reliable measurements. Deionized water (H_2O) was used for photodegradation experiments.

C. Proton NMR

To confirm H/D exchange for Urd and Thd in D_2O, proton nuclear magnetic resonance (NMR) measurements were performed. The samples were prepared by mixing Urd or Thd with D_2O and allowing them to stand for 24 h prior to measurement. Proton NMR spectra were acquired using a JEOL JNM-ECZ600R spectrometer. In the obtained spectra, a peak observed at 4.66 ppm is attributed to the solvent and is not related to the molecular protons of Urd or Thd. Signals corresponding to all CH, CH_2, and CH_3 groups of Urd and Thd are observed, whereas no signals are detected for the NH_2, NH, or OH protons. These results indicate that the exchangeable protons on these functional groups were completely replaced by deuterium. In our earlier work we confirmed this to also be the case for Cyd.[2]

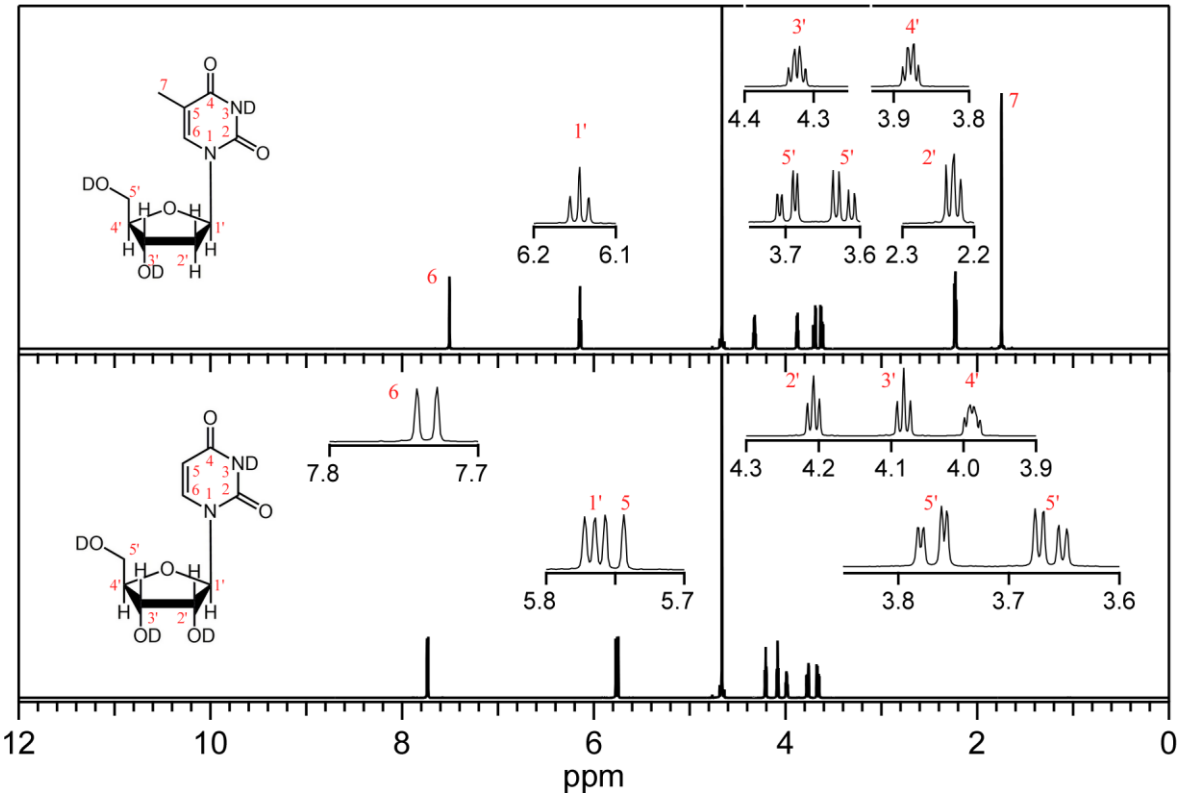

Figure S1. Proton NMR spectra of Urd (bottom) and Thd (top) in buffer solutions using D_2O.

D. Simulation of IR spectra

(a) IR spectra simulated using explicit solvent molecules

In aqueous solution at ambient temperature, the solvation structure of a solute is not unique but follows a statistical distribution. The experimentally observed IR spectrum therefore represents an ensemble average over multiple solute–solvent configurations. In principle, quantitative reproduction of such spectra requires configurational sampling based on molecular dynamics combined with quantum mechanics/molecular mechanics (QM/MM) calculations.

However, full QM/MM sampling is computationally prohibitive for the systems considered here and is beyond the scope of the present work. Instead, we approximate the IR spectra by performing harmonic vibrational frequency calculations on quantum-chemically optimized structures. To account for specific solute–solvent hydrogen-bonding interactions, strongly interacting water molecules are included explicitly in the quantum chemical calculations, while the surrounding bulk solvent is described using the polarizable continuum model (PCM). This approach represents a widely used compromise between computational feasibility and physical realism.

When explicit water molecules are included, the calculated vibrational frequencies depend on both the number and arrangement of these water molecules. Figure S2 illustrates this sensitivity for Thd.

The experimentally observed ground-state (planar) IR spectrum is compared with calculated spectra obtained under different assumptions regarding the number and positioning of explicit D_2O molecules. The C=O stretching band exhibits a systematic red shift as the number of hydrogen-bonded D_2O molecules increases, accompanied by changes in spectral shape. No single structural model fully reproduces the experimental spectrum, which is expected given the ensemble-averaged nature of the measurement.

It is important to emphasize that the primary objective of the spectrum calculations in this work is not to achieve quantitative reproduction of the entire experimental spectrum. Rather, the goal is to identify robust spectral signatures of a twisted intermediate (TI). In particular, we focus on (i) the blue shift of the C=O stretching band associated with the TI in Ura and Thy derivatives and (ii) the emergence of the ~1570 cm^{-1} marker band associated with the TI in Cyt derivatives. These features are consistently predicted irrespective of whether explicit D_2O molecules are included, demonstrating that the TI assignments are not sensitive to the specific solvation model.

As an exploratory analysis, we attempted to reproduce the experimental Thd spectrum by taking a linear combination of two calculated spectra: one without explicit D_2O molecules and one including three hydrogen-bonded D_2O molecules [Figure S3(a)]. Each vibrational band was broadened using Gaussian functions to approximate contributions from additional hydrogen-bonding configurations. As shown in Figure S3, this procedure yields a spectrum that reasonably resembles the experimental profile. When applied to multiple systems, the optimized weights of the two calculated components vary from molecule to molecule (Table S3). For some systems, the spectrum without explicit D_2O agrees more closely with the experimental spectrum, whereas for others the inclusion of explicit D_2O improves the agreement. In the main text and Figure S11, calculations for the Ura derivatives are presented without explicit D_2O molecules, whereas for the Thy and Cyt derivatives, calculations including explicit D_2O molecules are described. The same scaling factors and Gaussian broadening parameters given in Table S3 were applied in all cases. Identical values were used for both the planar and twisted ground-state structures.

This variability is consistent with differences in ensemble-averaged solvation structures among the solutes. Two conclusions follow:

1. The diagnostic TI marker bands are robust and can be clearly identified regardless of whether explicit water molecules are included (Figure S2).
2. Within the present harmonic framework (i.e., without configurational sampling), no single solvation model universally reproduces the experimental spectra for all systems. The remaining discrepancies are attributable to the statistical distribution of solvation structures.

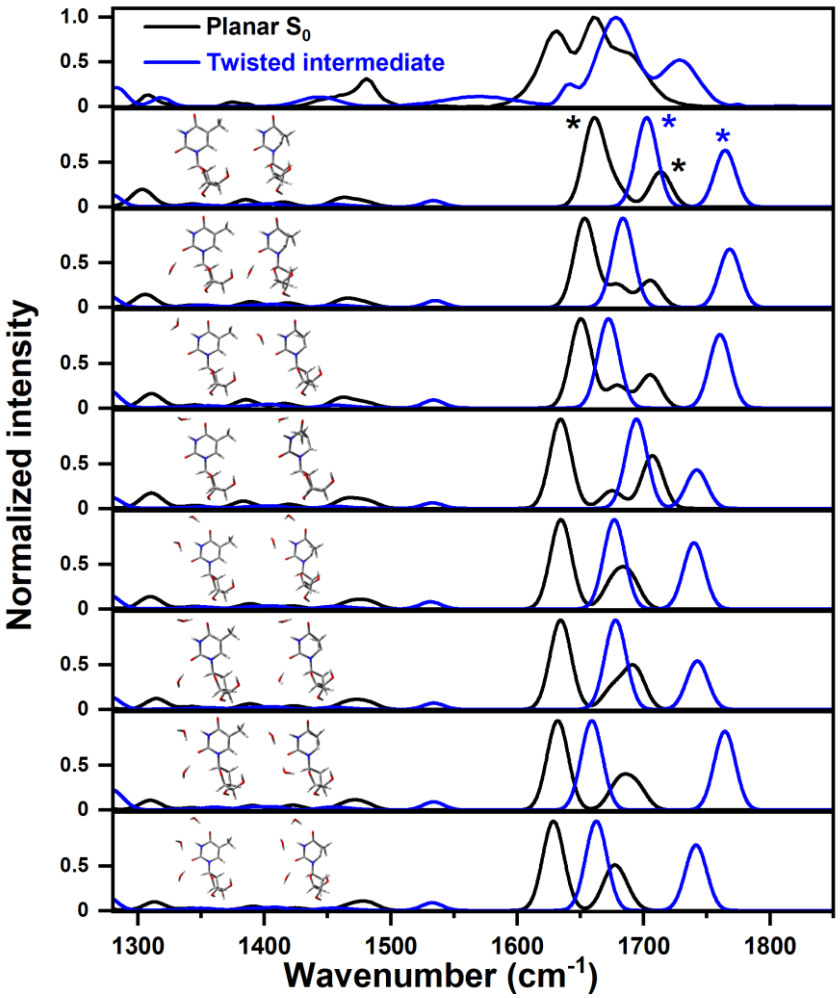

Figure S2. Calculated IR spectra of planar and twisted ground states of DThd using B3LYP/def2-TZVP with PCM (D_2O) level of theory, obtained under different assumptions regarding the number and positioning of explicit D_2O molecules (insets). Frequencies were scaled by a factor of 0.993 and a Gaussian function with a FWHM of 20 cm^{-1} was convolved with the corresponding stick spectra. The C=O stretching vibrations are marked with asterisks.

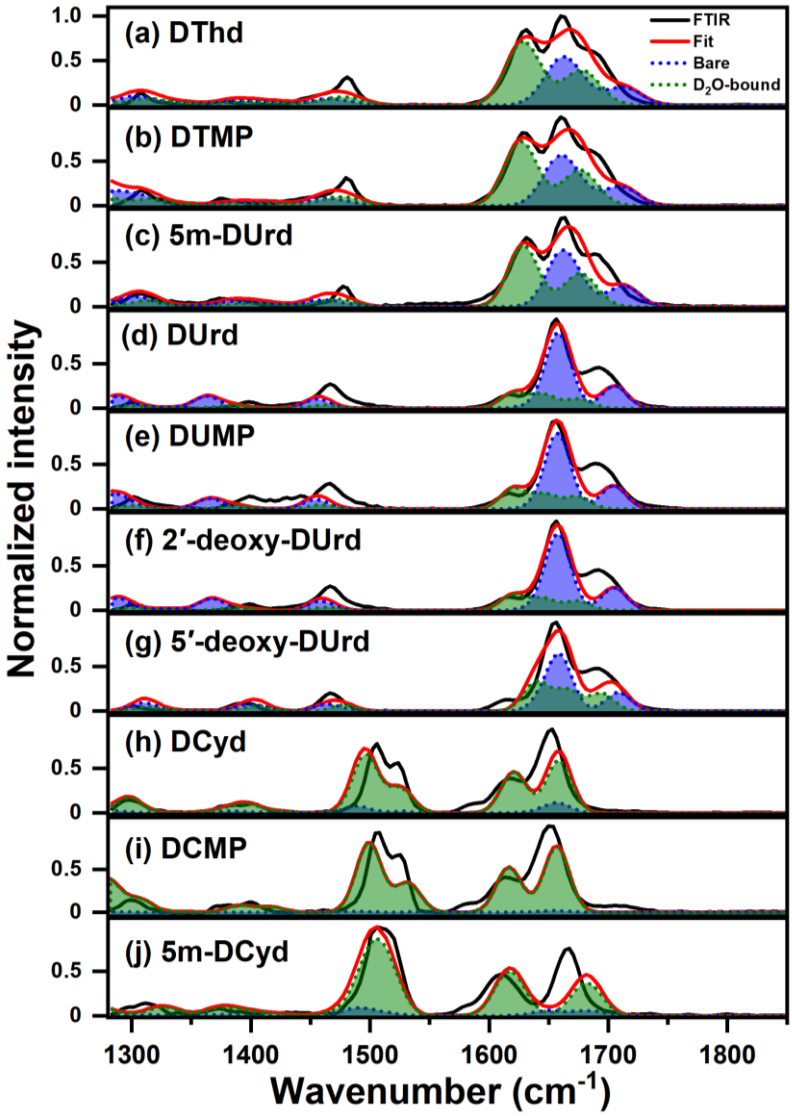

Figure S3. Least-squares fitting of experimental FTIR spectra using linear combination of two calculated spectra: one without explicit D_2O molecules and one including three (four for Cyt derivatives) hydrogen-bonded D_2O molecules. Calculations were performed at the B3LYP/def2-TZVP with PCM (D_2O) level of theory.

Table S3. Normalized weights, frequency scaling factors, and Gaussian broadening values obtained from least-squares fits shown in Figure S3.

Sample	Normalized weight		Frequency scaling factor	Gaussian broadening (cm^{-1})
	Bare	D_2O-bound		
DUrd	0.75	0.25	0.983	25
DThd	0.45	0.55	0.993	34
DCyd	0.10	0.90	0.988	25
DUMP	0.70	0.30	0.984	25
DTMP	0.46	0.54	0.993	33
DCMP	0.02	0.98	0.994	25
2′-deoxy-DUrd	0.75	0.25	0.984	25
5′-deoxy-DUrd	0.57	0.43	0.996	25
5m-DUrd	0.49	0.51	0.991	30
5m-DCyd	0.11	0.89	0.991	30

(b) Calculations for *syn*- and *anti*-rotamers

Syn- and anti-conformers of nucleosides (and -tides) arise from rotation about the N-glycosidic bond. We calculated the IR absorption spectra for both the planar and twisted ground states for all molecules, considering both *syn*- and *anti*-conformations. As shown in Figure S4, the spectra of the *syn*- and *anti*-forms are very similar.

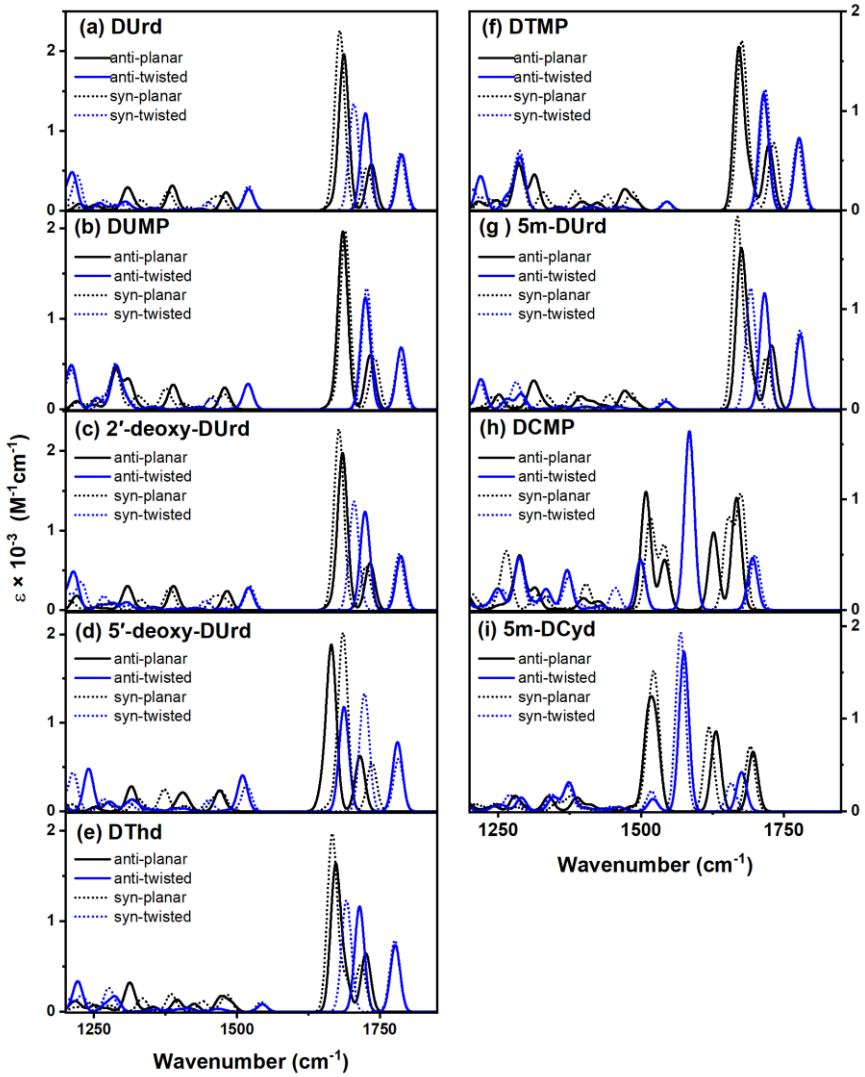

Figure S4. Calculated IR spectra for planar global minimum (black) and twisted intermediate (blue) for (a) DUrd, (b) DUMP, (c) 2′-deoxy-DUrd, (d) 5′-deoxy-DUrd (e) DThd, (f) DTMP, (g) 5m-DUrd, (h) DCMP, and (i) 5m-DCyd in D_2O. Theoretical calculations were performed using a harmonic model and DFT at the B3LYP /def2-TZVP+PCM(D_2O) level of theory, assuming the *anti*- (solid) and *syn*- (dashed) rotamers. In (h) and (i), four explicit D_2O molecules were additionally considered. No scaling was applied to the frequencies. A Gaussian function with a FWHM of 20 cm^{-1} was convolved with the corresponding stick spectra.

E. Photodegradation experiment

(a) Setup

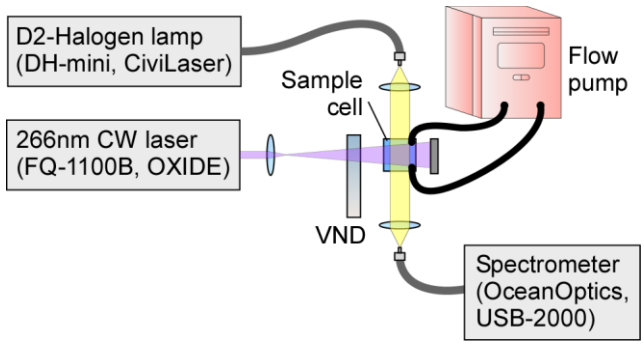

Figure S5. Schematic diagram of setup used for photodegradation experiment.

(b) Calculation of true photohydration rate and photohydration quantum yield

For our photodegradation experiments, the irradiation volume was $6.4 \times 10^{-4}\ L$ (V_{irrad}) and the incident photon rate per unit irradiation volume (I_0) was $1.88 \times 10^{21}\ photons \cdot L^{-1} \cdot min^{-1}$, respectively. We circulated sample solutions of 9.5 mL (V_{tot}). So, the effective irradiation fraction (f_{irrad}) is defined as,

$$f_{\mathrm{irrad}} = \frac{V_{\mathrm{irrad}}}{V_{\mathrm{tot}}} \tag{S1}$$

f_{irrad} is calculated to be 0.0674, and the true photohydration rate (k_{hyd}) is obtained by:

$$k_{hyd} = \frac{k_{obs} + k_{back}}{f_{\mathrm{irrad}}} \tag{S2}$$

where k_{back} is the dehydration rate constant, which is not negligible for Cyt, Cyd and CMP. We used k_{back} from literature.[3] The photohydration quantum yield Φ_{hyd} (number of hydration events per absorbed photon) is defined as:

$$\frac{d[Hydrate]}{dt} = \Phi_{hyd} \frac{I_{abs}}{N_A} \tag{S3}$$

Where N_A is Avogadro number and I_{abs} is the absorbed photon rate per unit irradiation volume [$I_{abs} = I_0\ (1 - 10^{-A})$]. The parent molecule decays as a (pseudo) first-order process:

$$-\frac{dC}{dt} = k_{hyd} C \tag{S4}$$

where C is the concentration of parent molecules. When absorption by the product is negligible, all photoabsorption is attributed to the parent:

$$k_{hyd} C = \Phi_{hyd} \frac{I_{abs}}{N_A} \tag{S5}$$

Thus:

$$\Phi_{hyd} = \frac{k_{hyd} C N_A}{I_{abs}} \quad \text{(S6)}$$

Using $C = \frac{A}{\varepsilon l}$, one can rewrite the formula purely in incident-photon terms:

$$\Phi_{hyd} = \frac{k_{hyd} N_A A}{\varepsilon\, l\, I_0 (1 - 10^{-A})} \quad \text{(S7)}$$

where ε, l, and A are the molar absorption coefficient, path length, and absorbance, respectively.

Table S4. Photohydration quantum yields

Sample	Φ_{hyd} (This work[a])	Φ_{hyd} (Ref. 3)
Ura	0.0026	0.0007 (at pH=6.2)
Urd	0.021	0.017
UMP (5′)	0.019	0.022 (2′ and 3′)
2′-deoxy-Urd	0.022	-
5′-deoxy-Urd	0.023	-
Thy	0.00015	0.000003 (at pH=6)
Thd	0.00030	-
TMP	0.00020	-
5m-Urd	0.00030	-
Cyt	0.005[b]	0.002[c]
Cyd	0.015[b]	0.01[c]
CMP	0.021[b]	0.0025[c]
5m-Cyd	0.0007	-

[a]in H_2O, at pH~7; [b]corrected for thermal reversal; [c]not corrected for thermal reversal

(c) Reversibility of photodegradation

Cytidine monophosphate (CMP)

Figure S6(a) shows UV spectra of CMP recorded over 10 min of photoirradiation with a photon flux of 1.88×10^{18} photons·cm^{-2}·min^{-1}. The absorption-band intensity decreases upon photoirradiation, but recovers substantially 25 min after irradiation [Figure S6(b)], in agreement with a previous report.[3] The photodegradation rate constant determined from the photoirradiation study [Figure S6(c)] was largely underestimated due to this reversibility, and was thus corrected using the back-reaction rates previously reported,[3] as described in the preceding section.

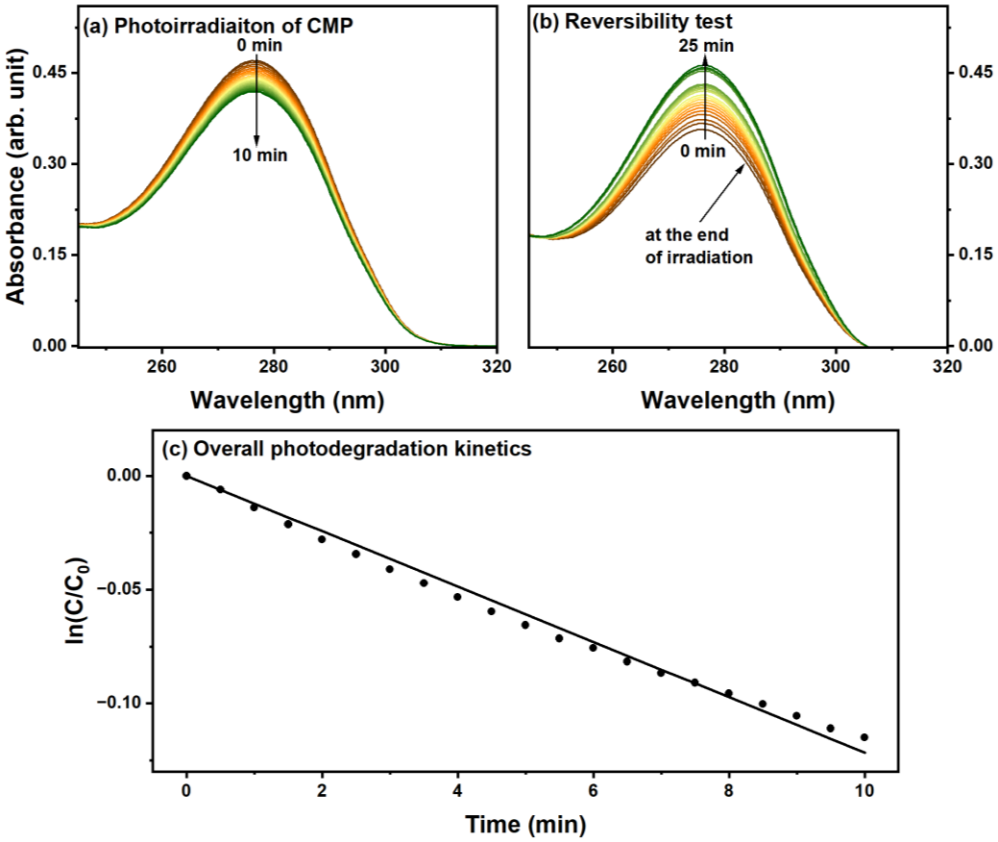

Figure S6. (a) Change in UV absorption spectrum of CMP with photoirradiation time using 266 nm CW UV laser with incident photon flux of 1.88×10^{18} photons·cm^{-2}·min^{-1}, and (b) spectral recovery due to thermal back-reaction. (c) Observed photodegradation (hydration) kinetics for CMP.

Cytidine (Cyd)

Figure S7(a) presents the results for recovery of UV absorption for Cyd due to thermal back-reaction following irradiation. After 1 h in the dark, partial recovery of the lowest-energy absorption band is observed; however, the extent of recovery is significantly smaller than that observed for CMP. These results indicate that photohydration of Cyd is only partially reversible under the present conditions.

Uridine (Urd)

Figure S7(b) shows the corresponding results for Urd. After 1 h in the dark following irradiation, the intensity of the lowest-energy absorption peak is not changed at all. Therefore, photohydration is not reversible, at least within the irradiation timeframe, and $\boldsymbol{k_{back}}$ in Equation S2 is negligible. Similar behavior was found for other Urd derivatives (not shown).

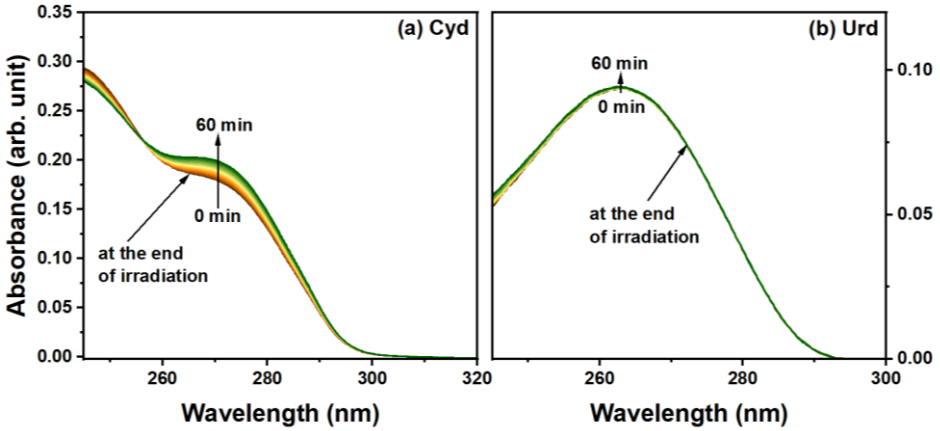

Figure S7. Recovery of UV absorption due to thermal back-reaction after irradiation is complete for (a) Cyd and (b) Urd.

(d) Additional photodegradation studies

Figure S8 shows the photodegradation results for several samples whose photodegradation (hydration) rate constants (k_{hyd}) are given in Table 4 in the main text.

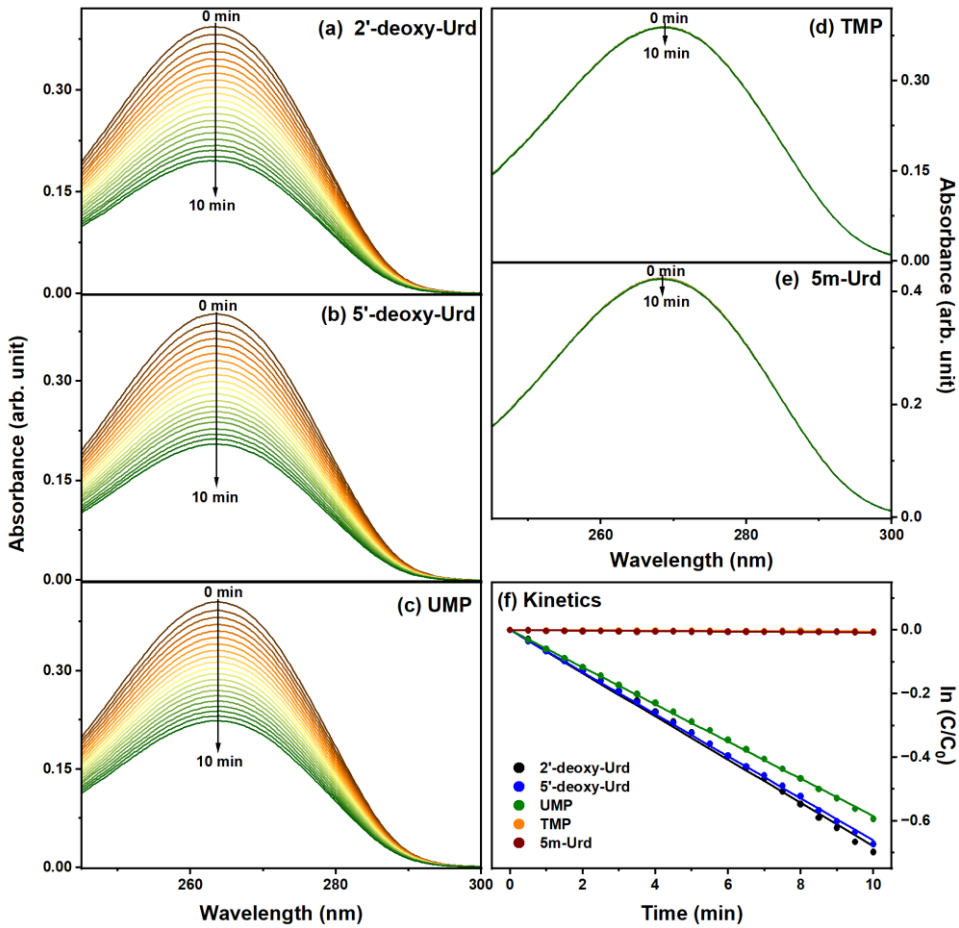

Figure S8. Results of photoirradiation experiments using 266 nm CW UV laser with incident photon flux of 1.88×10^{18} photons·cm^{-2}·min^{-1}. Changes in UV absorption spectra with time for (a) 2′-deoxyUrd, (b) 5′-deoxyUrd, (c) UMP, (d) TMP, and (e) 5m-Urd. (f) Resulting photodegradation (hydration) kinetics.

(e) Isotope effect on photodegradation

One way to confirm that the observed photodegradation corresponds to a hydration reaction is to change the solvent from H_2O to deuterated water (D_2O) and examine the kinetic isotope effect on the reaction rate. Although such measurements have been reported previously,[3] we re-examined this effect in the present work. The photodegradation process was found to be markedly slower in D_2O (Figure S9). The observed kinetic isotope effect was determined to be 2.4, which is comparable to the value of ~2 obtained previously.[3]

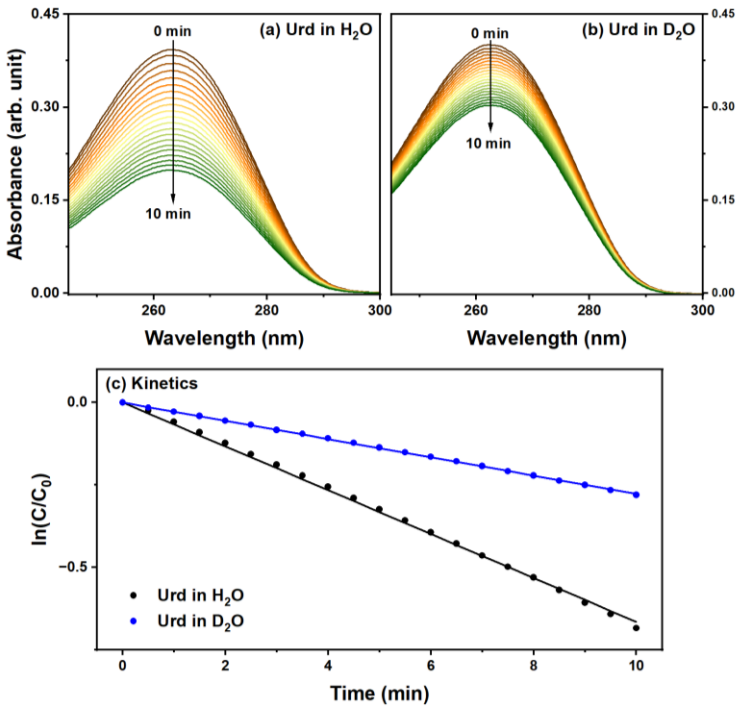

Figure S9. Photoirradiation with 266 nm CW UV laser with incident photon flux of 1.88×10^{18} photons·cm^{-2}·min^{-1}. Changes in UV absorption spectra with time for Urd in (a) H_2O and (b) D_2O. (c) Resulting photodegradation (hydration) kinetics.

(f) Effect of sugar moiety on photodegradation

Figure S10 compares the photodegradation of Urd and Ura to evaluate the influence of the sugar moiety on the reaction. Ura exhibits much slower photodegradation than Urd, highlighting the significant role of the sugar group.[3] The difference arises mainly from the different lifetimes of their TI, as discussed in the main text.

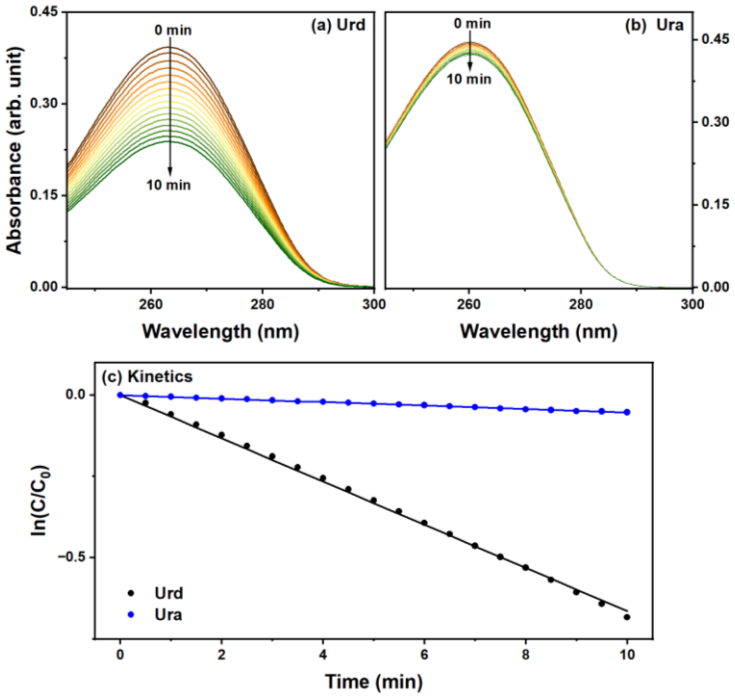

Figure S10. Photoirradiation with 266 nm CW laser with incident photon flux of 1.88×10^{18} photons·cm^{-2}·min^{-1}. Changes in UV absorption spectra with time for (a) Urd and (b) Ura. (c) Resulting photodegradation (hydration) kinetics.

(g) Kinetic analysis of hydration reaction

Under constant UV irradiation, the S_1 and TI populations are described by the following kinetic equations:

$$\frac{d[S_1]}{dt} = \sigma I[NB] - (k_T + k')[S_1] \quad (S8)$$

$$\frac{d[TI]}{dt} = k_T[S_1] - \frac{1}{\tau}[TI] - k_{hyd}[TI][H_2O] \quad (S9)$$

Here, $[NB]$, $[S_1]$, and $[TI]$ denote the concentration of nucleobases in the S_0 state (thermal equilibrium), S_1 state, and the TI, respectively, and $[H_2O]$ is the concentration of water. σ is the photoabsorption cross-section, I is the excitation photon flux, k_T is the formation rate for the TI, and k' is the rate constant for all other relaxation processes from S_1. τ is the lifetime of the TI for isomerization to the

planar structure, and k_{hyd} is the bimolecular hydration reaction rate constant. Because the concentration of H_2O can be regarded as constant, the bimolecular term can be approximated as pseudo-first order:

$$k_{hyd}[\mathrm{H_2O}] = k'_{hyd} \tag{S10}$$

Previous studies have shown that the quantum yield (QY) for the hydration reaction is 0.01 or smaller, indicating that $k'_{hyd} \ll 1/\tau$. Under this condition, application of the steady-state approximation to [TI] yields:

$$[\mathrm{TI}] \approx \tau k_T[\mathrm{S_1}] \tag{S11}$$

Similarly, applying the steady-state approximation to $[\mathrm{S_1}]$ gives:

$$[S_1] = \frac{\sigma I}{(k_T + k')}[\mathrm{NB}] \tag{S12}$$

Substituting Eq. (S12) into Eq. (S11), we obtain

$$[\mathrm{TI}] = \frac{\tau k_T \sigma I[\mathrm{NB}]}{(k_T + k')} = \tau \Phi \sigma I[\mathrm{NB}] \tag{S13}$$

where $\Phi = k_T/(k_T + k')$ is the QY for formation of the TI. Experimentally, the photohydration rate constant is determined from

$$\frac{d[\mathrm{HP}]}{dt} = k_{obs}[\mathrm{NB}] = k'_{hyd}[\mathrm{TI}] \tag{S14}.$$

where [HP] is the concentration of the hydration product. From Eqs. (S13) and (S14), we obtain

$$k_{obs} = \tau \Phi \sigma I k'_{hyd} \tag{S15}$$

In our measurements of the hydration reaction rate, the rate constant was obtained by adjusting the photoabsorption strength (or optical density of the liquid), so that we have the following relation:

$$k'_{obs} = C_0 \tau \Phi k'_{hyd} \tag{S16}$$

Here, C_0 is a common constant. Thus, under the same photon flux, the relative hydration reaction rate can be expressed as:

$$k'_{hyd} \propto \frac{k'_{obs}}{\tau \Phi} \tag{S17}$$

As mentioned in the section E (c), k'_{obs} must be corrected for the back reaction, when it is not negligible.

F. IR-TAS

(a) Additional nucleosides

In the main text, we considered the dynamics of 2′-deoxy-DUrd, 5′-deoxy-DUrd, and 5m-DUrd. The IR-TA spectra, selected lineouts, steady-state IR absorption spectra, species-associated spectra (SAS), and quantum chemical calculation results for the TI for these samples are shown in Figure S11. The dynamics of 2′-deoxyDUrd and 5′-deoxyDUrd closely resemble those of DUrd, whereas 5m-DUrd exhibits dynamics similar to DThd. These observations suggest that substitution of the –OH group at the 2′ and 5′ positions does not significantly influence the nucleoside dynamics.

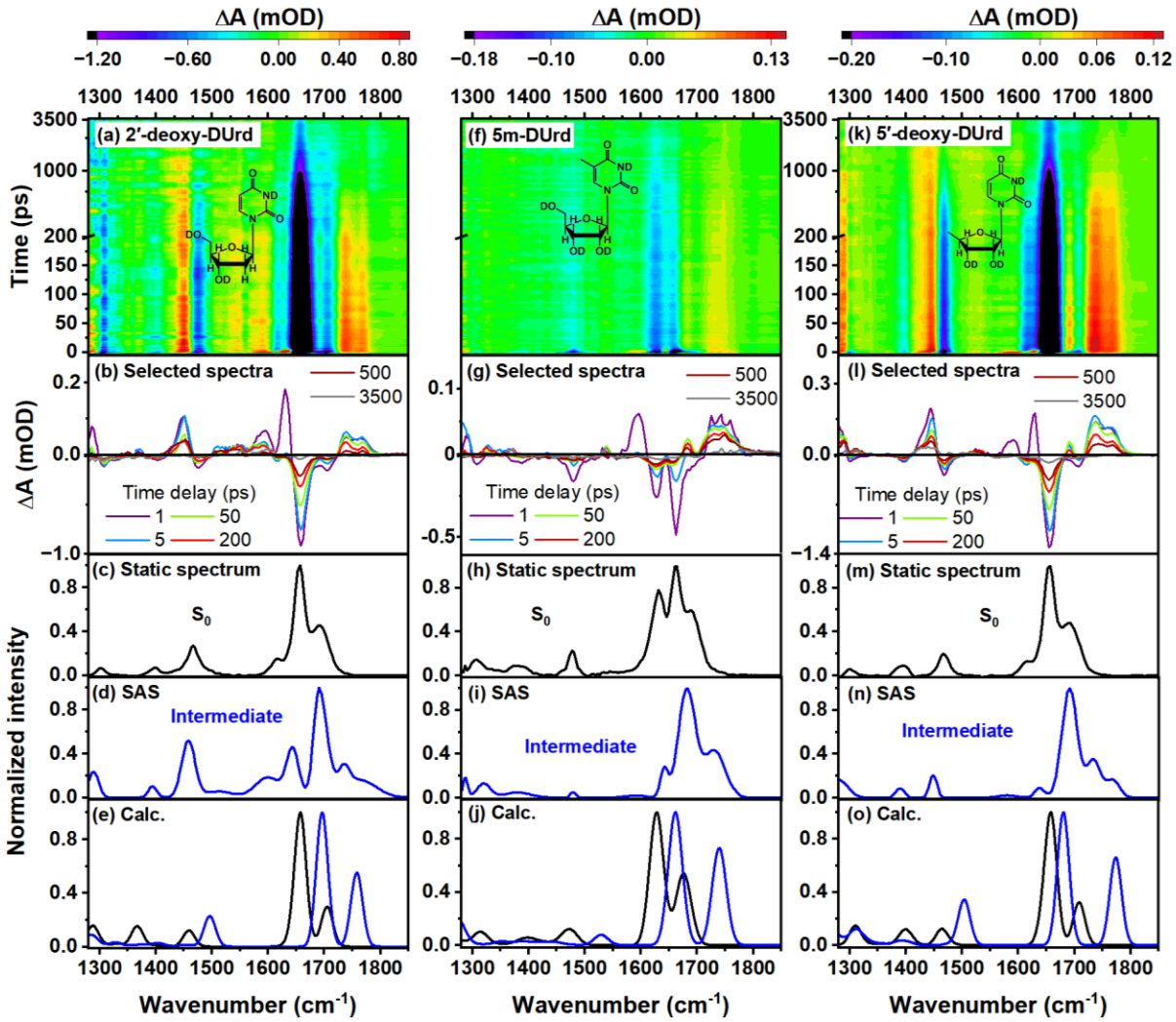

Figure S11. IR-TA spectra measured under 267 nm photoexcitation (a, f and k), selected lineouts (b, g and l), static IR spectra measured for S_0 (c, h, and m), IR spectra of intermediate species (d, i, and n), and theoretical IR spectra for global minimum (S_0) and TI (e, j and o), for 2′-deoxyDUrd, 5m-DUrd, and 5′−deoxyDUrd in PB-D_2O (20 mM). In (e), (j) and (o), the theoretical calculations were performed using a harmonic model and DFT at the B3LYP /def2-TZVP+PCM (D_2O) level of theory, assuming an *anti*-rotamer. Three explicit D_2O molecules were considered additionally for (j). The calculated frequencies were scaled and stick spectra were convoluted with a Gaussian function, as detailed in Section D(a) and summarized in Table S3.

(b) Ground state bleach recovery (GSBR)

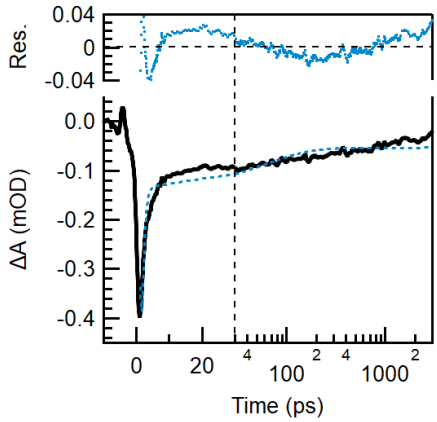

Figure S12. GSBR waveform (black solid line) at 1630 cm^{-1} and single exponential fit (blue dashed line) for 5m-DUrd. The waveform exhibits complex features in the negative time range due to the free induction decay in the probe-pump pulse sequence. The horizontal scale is linear up to 30 ps and logarithmic thereafter.

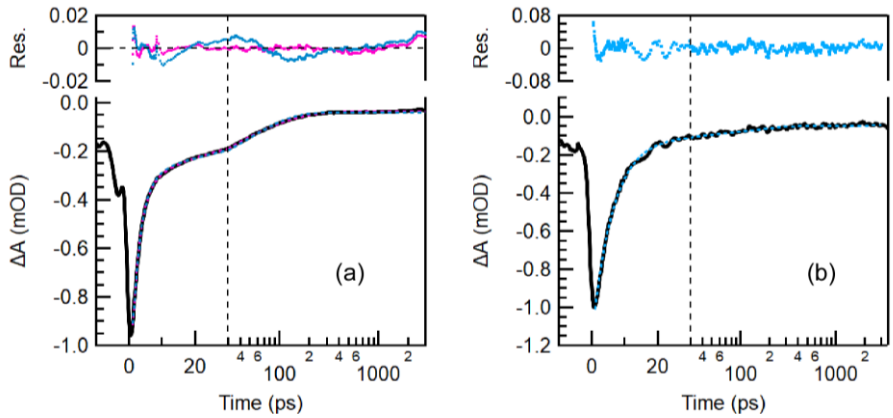

Figure S13. GSBR waveforms (black solid line) and exponential fits for (a) DCMP (1650 cm^{-1}) and (b) 5m-DCyd [obtained from the analysis described in Section F(e) and Figure S18]. Blue and pink dashed lines show least-squares fits assuming single and dual exponential decay for the intermediate, respectively, in addition to direct internal conversion to S_0 and cascaded relaxation via the triplet state. The waveforms exhibit complex features in the negative time range due to the free induction decay in the probe-pump pulse sequence. The horizontal scale is linear up to 30 ps and logarithmic thereafter.

(c) Vibrational frequency dependence of GSBR and positive marker-band dynamics

In the main text and the preceding sections of this Supporting Information, the dynamics and fitting results were presented for ground state bleach recovery (GSBR) at the strongest IR band for all samples. Here, we describe the variation of the GSBR and the positive marker-band waveforms with the

vibrational frequency along with fitting results (Figures S14 and S15). The fitting parameters are summarized in Tables S5 and S6. The range of variability of the parameters is smaller at the GSB minimum than the maximum of the positive band. This is likely because the absolute signal intensity is larger for the GSB than for the positive band, reducing the influence of band overlap. Consistent results were also obtained for other Urd derivatives. Therefore, we adopted the time constants derived from the GSBR fits as those representing the intermediate states.

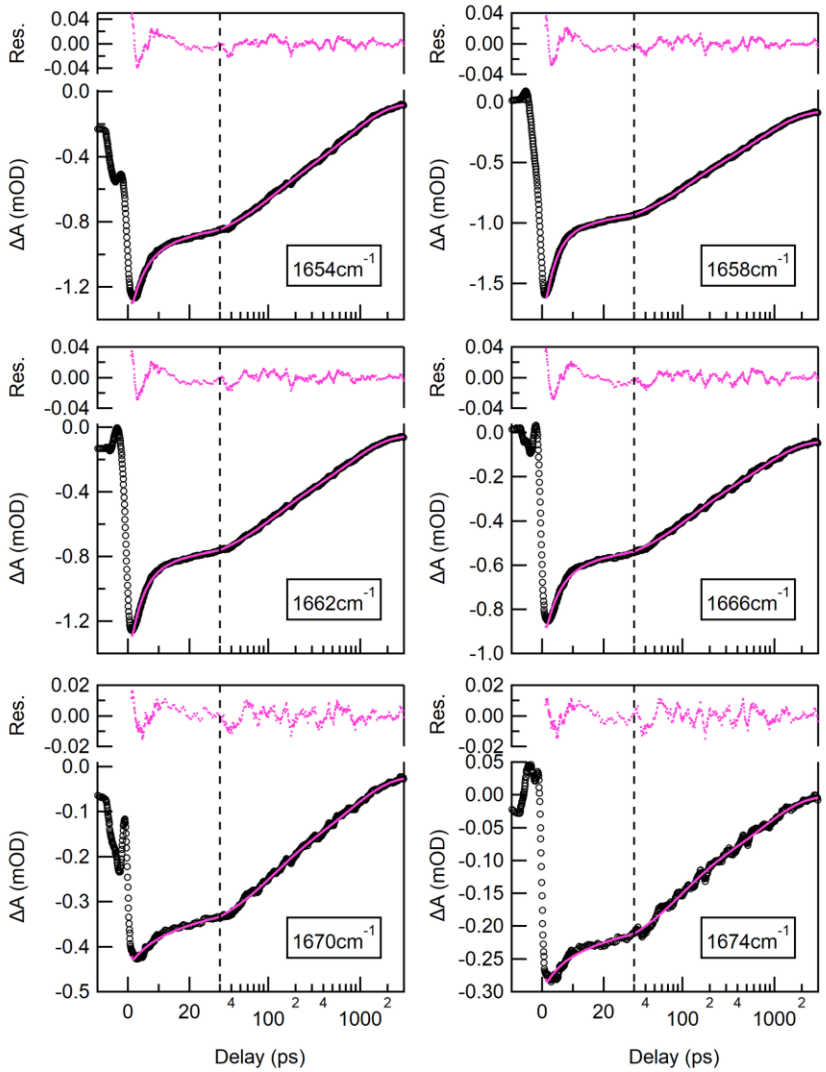

Figure S14. GSBR waveforms for different wavenumbers and corresponding exponential fits for DUrd.

Table S5. Fitted kinetic parameters obtained from wavenumber-dependent GSBR waveforms shown in Figure S14 for DUrd. Outside these wavenumber regions, overlapping positive bands or reduced signal intensity prevented meaningful fitting results from being obtained.

Wavenumber (cm^{-1})	τ_{hot} (ps)	τ_{TI}^{1}(ps)	τ_{TI}^{2} (ps)	τ_{trp} (ps)	a_{hot}	a_{TI}^{1}	a_{TI}^{2}	a_{trp}
1654	5	85	740	>3500	0.32	0.24	0.38	0.05
1658	4	85	738	>3500	0.42	0.22	0.31	0.04
1662	4	87	727	>3500	0.4	0.23	0.33	0.04
1666	5	91	729	>3500	0.36	0.26	0.33	0.04
1670	7	90	785	>3500	0.13	0.38	0.44	0.05
1674	6	82	776	>3500	0.15	0.42	0.42	0.01

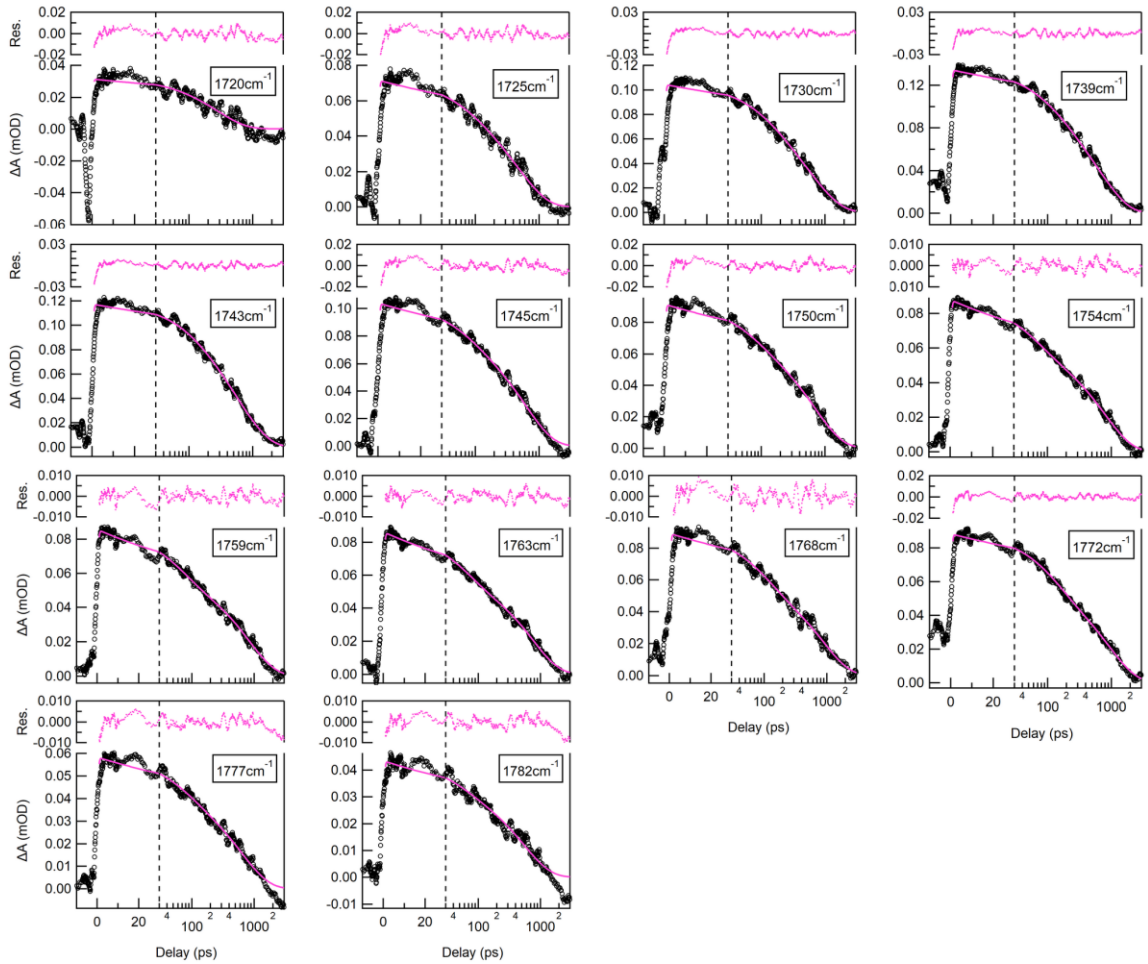

Figure S15. Positive marker-band waveforms for different wavenumbers and corresponding exponential fits for DUrd.

Table S6. Fitted kinetic parameters obtained from wavenumber-dependent positive marker-band waveforms shown in Figure S15 for DUrd.

Wavenumber (cm^{-1})	τ_{TI}^{1} (ps)	τ_{TI}^{2} (ps)	a_{TI}^{1}	a_{TI}^{2}
1734	105	621	0.21	0.79
1739	127	707	0.25	0.75
1743	156	706	0.23	0.77
1745	71	621	0.23	0.77
1750	76	712	0.26	0.74
1754	59	792	0.32	0.68
1759	63	830	0.35	0.65
1763	59	756	0.35	0.65
1768	96	882	0.36	0.64
1772	121	947	0.35	0.65
1777	75	656	0.28	0.72
1782	53	546	0.25	0.75

(d) Feasibility of differentiating isomers of twisted intermediate

As discussed in the main text and in the preceding subsection of this Supporting Information, the back-reaction from the TI to the planar structure in the S_0 state exhibits biexponential kinetics. Nucleosides and nucleotides can adopt *syn*- and *anti*-rotamer configurations; however, NMR studies indicate that the *anti*-rotamer is dominant. Thus, we speculated that the observed duality in the back-reaction rates may originate from ribose ring puckering. Testing this hypothesis will require future studies using locked nucleic acids in which ribose puckering is constrained. As an alternative attempt, we examined whether the spectral signatures of the TI could be separated into two independent species. For this purpose, DUrd, characterized by a relatively high QY for the TI, was selected as a representative system. Global fitting was performed on the IR-TAS data in the time window following rapid vibrational relaxation in aqueous solution, assuming two components for the TI, in addition to the triplet state. This analysis yielded an additional decay-associated difference spectrum (DADS) with a lifetime of approximately 100 ps, alongside the dominant component with a lifetime exceeding 500 ps. As shown in Figure S16(a), the two normalized SAS are nearly identical in the high-frequency region, indicating that reliable separation into two spectrally distinct components is difficult.

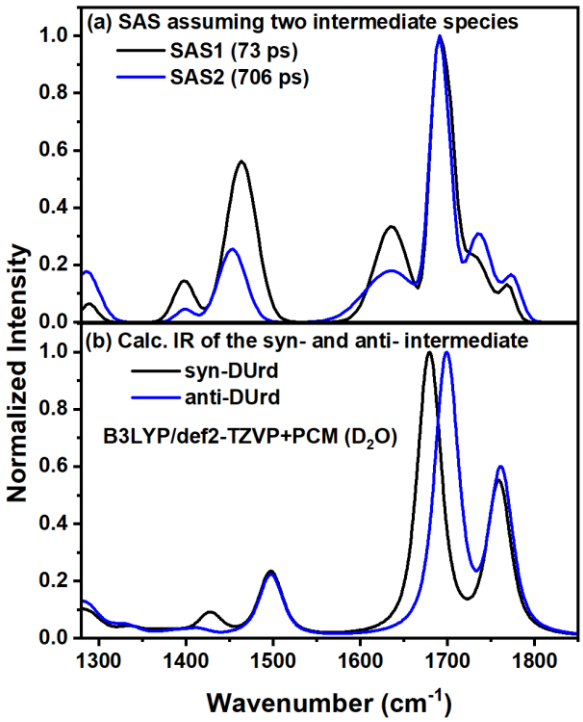

Figure S16. (a) IR absorption spectra obtained by global fitting with additional component for TI; (b) Computational IR spectra of *syn*- and *anti*-rotamers of TI at B3LYP/def2-TZVP+PCM (D_2O) level of theory. All the calculated frequencies were scaled by 0.985 (obtained by matching the peak positions at the ground-state minima). A Gaussian function with a FWHM of 20 cm^{-1} was convolved with the corresponding stick spectra.

(e) Detailed analysis for 5m-DCyd

The $^1\pi\pi^*$ state of 5m-DCyd exhibits a longer lifetime than those of the other compounds, requiring a slightly different analysis. We first performed global fitting in the region from 10 ps onwards using a three-component parallel kinetic model, and obtained three DADS. The infinite-lifetime component corresponds to the triplet state, the ~8 ps component to the $^1\pi\pi^*$ state, and the intermediate-lifetime component to the TI. To extract an accurate DADS for the TI, global fitting was again performed from 30 ps onward, where the contribution of the 8 ps $^1\pi\pi^*$ state becomes negligible. The positive peak observed in the IR-TAS spectrum up to ~150 ps is primarily attributed to the TI. Its excellent agreement with theoretical calculations (main text, Figure 6) allowed unambiguous assignment. The resulting SAS are shown in Figure S17.

To account for the influence of the $^1\pi\pi^*$ state of 5m-DCyd, we then refitted the full dataset using the obtained SAS, the ground-state IR spectrum, and additional spectral components representing vibrational relaxation of the vibrationally excited state in S_0 using the following expression:

$$S(\nu,t) = -c_{gs}(t)GS(\nu) + c_t(t)P(\nu) + c_I(t)I(\nu) + c_I(t)T(\nu) + c_\delta(t)D(\nu) \qquad \text{(S18)}$$

where c_j are expansion coefficients, $GS(\nu)$ is the steady state IR absorption, and $P(\nu)$, $T(\nu)$ and $I(\nu)$ are the SAS for the $^1\pi\pi^*$ state, triplet state, and the TI described above, respectively. $D(\nu)$ is the residual, which is expressed as a linear combination of Gaussian functions. Contributions from $T(\nu)$ at times less than 10 ps and from $P(\nu)$ at times beyond 30 ps are negligibly small, and hence they were not considered in these particular regions for fitting.

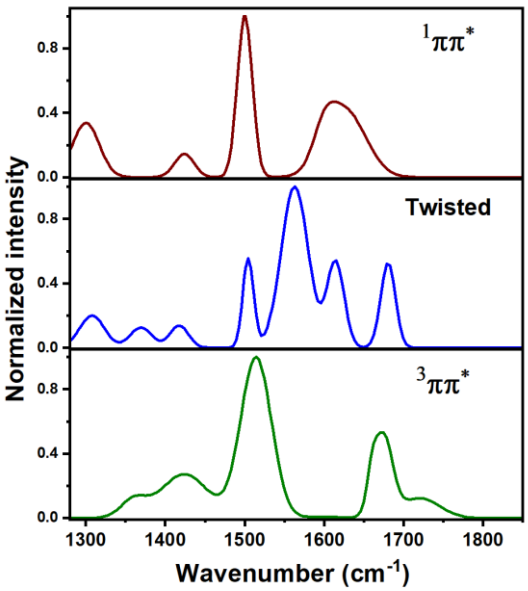

Figure S17. Extracted SAS for different species formed during electronic relaxation of 5m-DCyd.

The temporal evolution of the expansion coefficients (Figure S18) demonstrates that the decay of the $^1\pi\pi^*$ state is followed by the formation of the TI, while the triplet component remains constant. Compared with DCyd,[2] the TI in 5m-DCyd exhibits a longer rise time of approximately 4 ps (inset in Figure S18). A similar rise time of ~3 ps was obtained for the isolated positive band at 1559 cm^{-1}, assigned to the intermediate (Figure S19). The term $-\boldsymbol{c_{gs}(t)}$, which can be treated as ground state bleach recovery kinetics, was analyzed to determine the QYs and time constants for various relaxation channels (Table 1 in the main text), and $\boldsymbol{\Phi_{TI}}$ and $\boldsymbol{\tau_{TI}}$ values of 0.06 and 122 ps, respectively, were obtained.

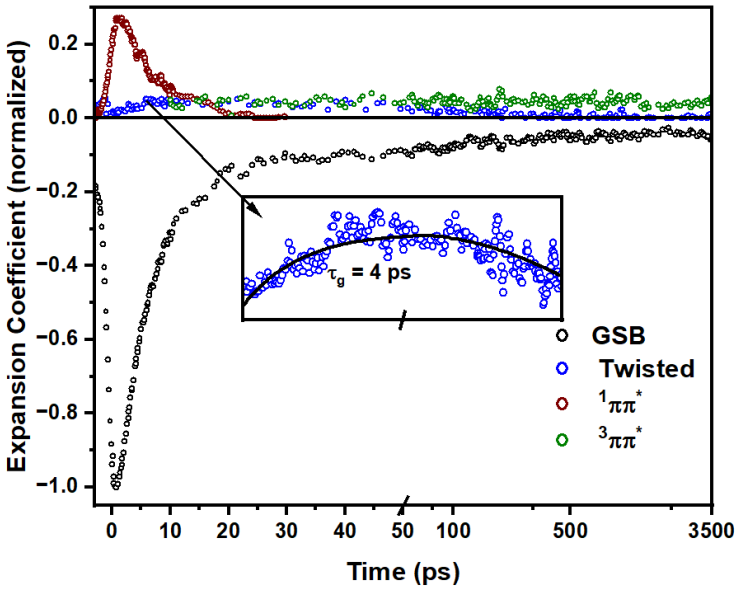

Figure S18. Temporal evolution of different species formed during electronic relaxation of 5m-DCyd. The inset presents a zoomed trace for the TI, showing its formation dynamics.

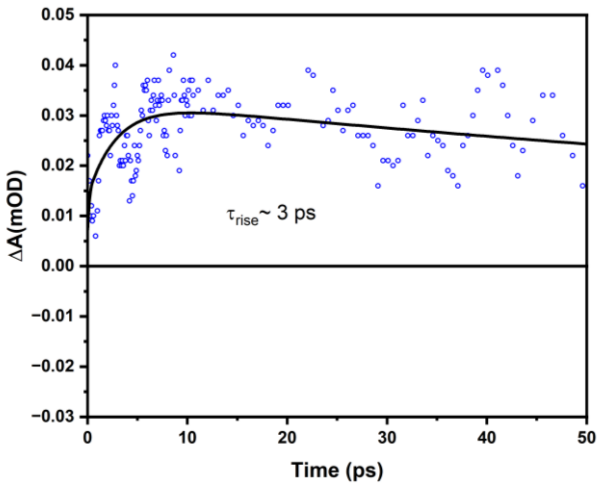

Figure S19. Temporal evolution of 1559 cm^{-1} positive band for 5m-DCyd.

G. QM/MM

(a) Setup

To perform mixed quantum-classical molecular dynamics simulations and geometry optimization for critical points, each system is partitioned as shown in Figure S20. The nucleobase (high layer) is treated at the QM level. The sugar and closest water molecules (medium layer) comprising the first two solvent

shells are treated at the MM level and are allowed to move during the dynamics. Finally, the remaining water molecules (low layer) are also treated at the MM level but they are kept frozen during the dynamics.

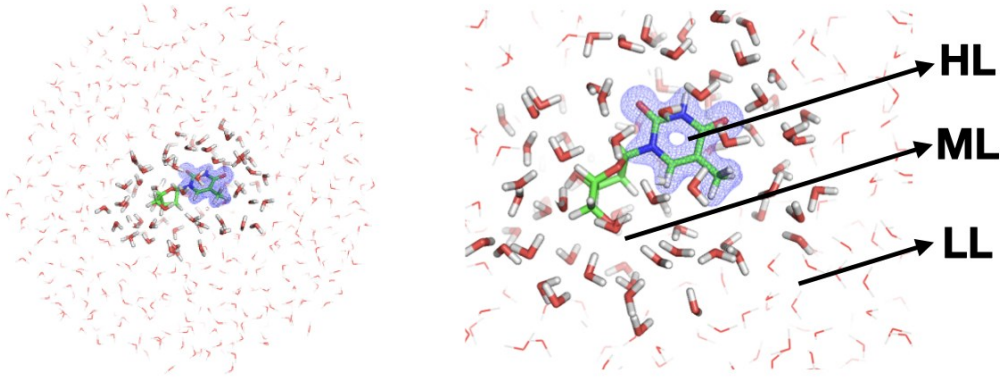

Figure S20. Thd fully solvated in water droplet (left). Enlarged view illustrating QM/MM partitioning into high (HL), medium (ML) and low (LL) layers (right).

(b) Active space (dynamics)

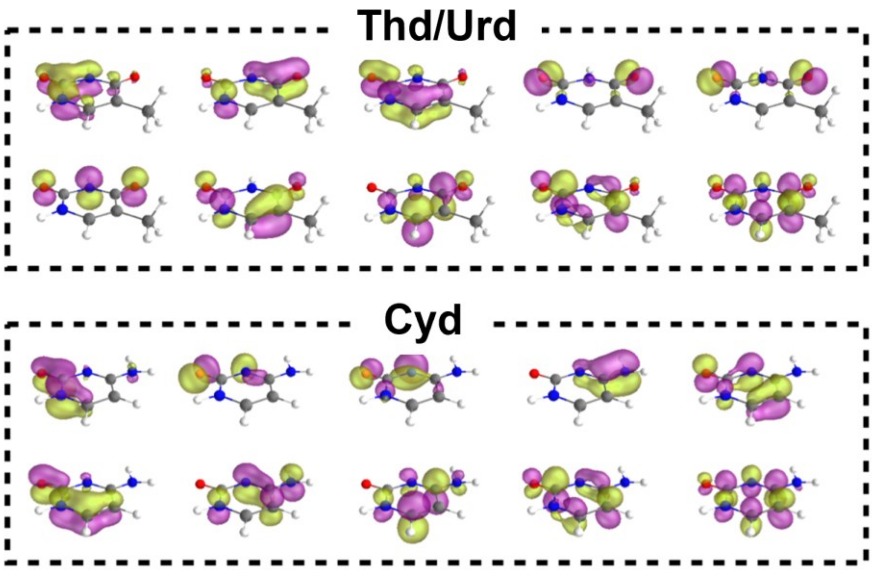

Figure S21. (14,10) active space employed in QM region for Thd and Urd (top), and Cyd (bottom).

(c) Active space (RMS-CASPT2)

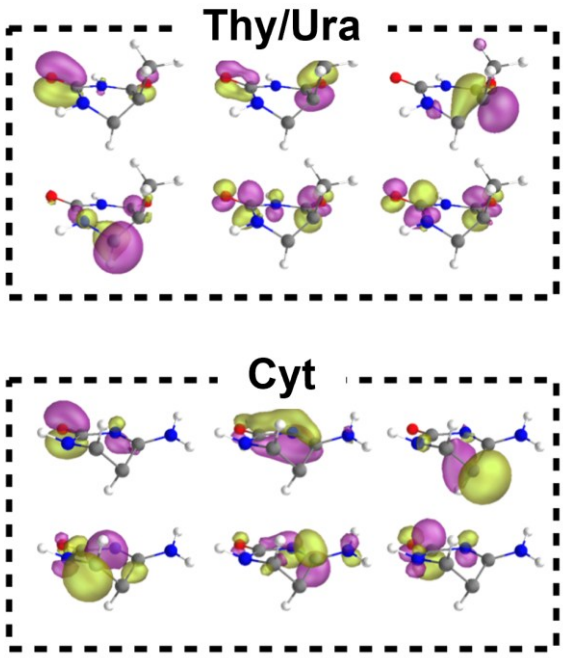

Figure S22. (6,6) active space employed for static analysis of Thy and Ura (top), and Cyt (bottom).

The accuracy of the (6,6) active space relative to the (14,10) active space was assessed by comparing relative energies and structures computed at key critical points, namely the TI minimum and the transition states of Ura, Thy and Cyt in the gas phase, as shown in Figure S23. As can be seen, the effect of the active space for the optimized geometries is negligible and the relative trend in the activation barrier is also similar. In particular, the ratios of the computed barriers within the small active space are conserved reasonably well when using the larger one.

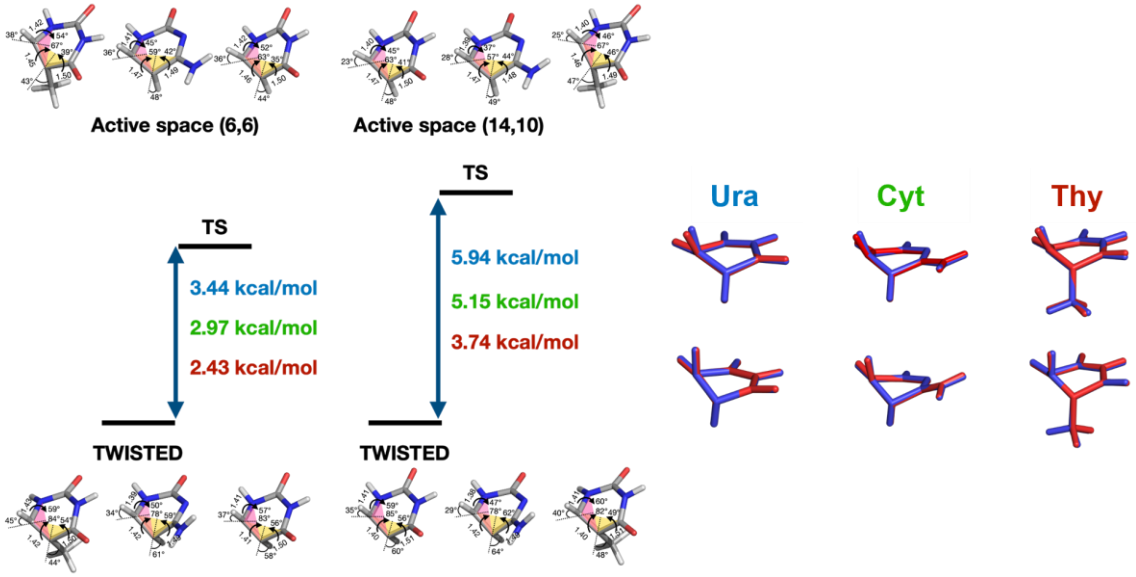

Figure S23. Computed energy barrier and structures for TI and transition states for Thy, Cyt and Ura using (6,6) and (14,10) active spaces. Superimposed geometries are also shown in blue for the (6,6) active space and in red for the (14,10) active space.

(d) Construction of reactive PES

The reactive 2D-PES was constructed by linear interpolation in internal coordinates. The plane was constructed to fully contain the three key structures of Ura [Figure 7(d)] and Thy [Figure 7(f)] optimized in the gas phase: the ground-state planar minimum ($Planar_{min}$), the minimum TI ($Twisted_{min}$) and the minimum energy of the S_1/S_0 conical intersection (MECI). All three structures were converted from Cartesian coordinates to the internal coordinates shown below.

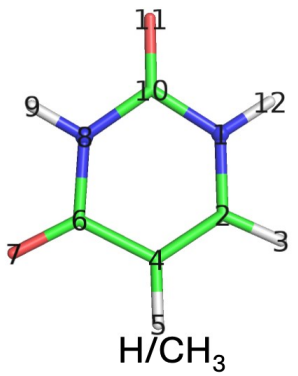

Figure S24. Indices of atoms referred to in Tables S7 and S8. It should be noted that the numbering of atoms is different from that in Figure 1 in the main text.

Table S7. Coordinates used for constructing Figure 7(d) for Ura in the main text.

	$Planar_{min}$	MECI	$Twisted_{min}$	TS	X
Bond: 2 1	1.382061	1.326653	1.414654	1.420274	1.40325
Bond: 3 2	1.092274	1.101193	1.100943	1.100624	1.09791
Bond: 4 2	1.363991	1.459797	1.409829	1.459083	1.39379
Bond: 5 4	1.089268	1.12039	1.100331	1.10141	1.09646
Bond: 6 4	1.463992	1.472209	1.502247	1.498085	1.48886
Bond: 7 6	1.229902	1.219925	1.212951	1.220727	1.21888
Bond: 8 6	1.413052	1.46396	1.427998	1.409085	1.42277
Bond: 9 8	1.023878	1.025343	1.024248	1.02421	1.02412
Bond: 10 8	1.390778	1.372409	1.420054	1.408711	1.40981
Bond: 11 10	1.226128	1.217218	1.21965	1.221412	1.22192
Bond: 12 1	1.019108	1.029044	1.024841	1.024694	1.02283
Angle: 3 2 1	115.531019	116.213641	118.767264	118.081277	117.635
Angle: 4 2 1	121.701234	118.25638	106.559431	107.871282	111.859
Angle: 5 4 2	121.440523	102.586365	113.000475	118.257702	115.954
Angle: 6 4 2	119.78632	113.573472	107.647451	113.514087	111.896
Angle: 7 6 4	126.020516	130.015167	134.901276	128.574241	131.793
Angle: 8 6 4	113.377057	112.41043	101.581968	108.775838	105.71
Angle: 9 8 6	116.243999	114.769241	117.907305	116.923148	117.325
Angle: 10 8 6	128.609522	123.794921	128.39286	127.374527	128.469
Angle: 11 10 1	123.156092	118.547929	122.836638	123.250879	122.948
Angle: 12 1 2	121.191811	123.92443	121.808009	120.069429	121.592
Torsion: 3 2 1 10	179.954536	146.304293	86.322971	91.989794	119.094
Torsion: 5 4 2 1	-179.98768	-61.326598	-39.267687	-72.070637	-88.5197
Torsion: 6 4 2 1	0.018455	46.120289	83.179133	63.633013	54.0729
Torsion: 7 6 4 2	179.976491	171.630424	127.581618	148.308325	145.92
Torsion: 8 6 4 2	0.001846	-16.016465	-55.807791	-35.903108	-36.2744
Torsion: 9 8 6 4	-179.95286	-170.22043	-165.41519	-169.28702	-170.503
Torsion: 10 8 6 4	-0.025645	-22.37775	14.030417	-3.530288	9.1108
Torsion: 11 10 1 2	-179.9049	-173.90133	-162.98918	-162.70694	-168.91
Torsion: 12 1 2 3	-0.136813	-7.832186	-47.205911	-47.865053	-30.7317

Table S8. Coordinates used for constructing Figure 7(f) for Thy in the main text.

	$Planar_{min}$	MECI	$Twisted_{min}$	TS	X
Bond: 2 1	1.3824	1.3143	1.4270	1.4250	1.4149
Bond: 3 2	1.0928	1.1041	1.1028	1.1018	1.1001
Bond: 4 2	1.3698	1.4561	1.4164	1.4521	1.4038
Bond: 5 4	1.5013	1.5924	1.5068	1.5121	1.5053
Bond: 6 4	1.4651	1.4637	1.4974	1.4954	1.4887
Bond: 7 6	1.2346	1.2206	1.2164	1.2216	1.2213
Bond: 8 6	1.4092	1.4738	1.4246	1.4097	1.4204
Bond: 9 8	1.0233	1.0251	1.0245	1.0243	1.0242
Bond: 10 8	1.387	1.3648	1.4245	1.4100	1.4143
Bond: 11 10	1.2252	1.2169	1.2212	1.2221	1.2223
Bond: 12 1	1.0187	1.0290	0.9846	1.0245	0.9938
Angle: 3 2 1	115.41	115.2100	116.7100	117.4500	116.3600
Angle: 4 2 1	122.52	120.0600	105.5300	107.8600	110.1100
Angle: 5 4 2	123.8	103.9600	121.3600	120.6600	122.0200
Angle: 6 4 2	117.9	112.0500	107.4500	111.9300	110.2700
Angle: 7 6 4	124.73	130.0800	134.1000	128.7900	131.5700
Angle: 8 6 4	114.8	113.0200	102.1100	108.4300	105.5400
Angle: 9 8 6	116.28	115.4700	117.7500	117.1300	117.3600
Angle: 10 8 6	128.31	124.4000	128.4700	127.5100	128.4300
Angle: 11 10 1	123.36	117.9800	123.6200	123.4000	123.5500
Angle: 12 1 2	121.08	125.0000	120.7900	120.2600	120.8700
Torsion: 3 2 1 10	-179.92	149.2000	76.2500	87.9500	104.2400
Torsion: 5 4 2 1	-179.98	-59.8900	-51.9100	-69.6300	-86.4800
Torsion: 6 4 2 1	-0.04	47.4500	83.7900	67.1700	61.1500
Torsion: 7 6 4 2	-179.96	171.3500	131.6800	147.9600	144.7100
Torsion: 8 6 4 2	0.06	-20.5200	-53.9700	-38.6200	-39.3800
Torsion: 9 8 6 4	-179.9	-168.0300	-163.0700	-168.0800	-167.6200
Torsion: 10 8 6 4	-0.17	-16.7800	10.0700	-1.4400	7.3100
Torsion: 11 10 1 2	-179.86	-176.6600	-163.4200	-162.4700	-167.8600
Torsion: 12 1 2 3	-0.2	-8.8500	-59.2200	-49.5400	-43.2800

The plane is defined by two orthogonal vectors Q_1 and Q_2 in internal coordinates. Vector Q_1 points from the ground-state planar minimum $Planar_{min}$ to the TI $Twisted_{min}$. Vector Q_2 is the component of displacement orthogonal to Q_1 that brings $Planar_{min}$ to MECI. To construct Q_2, first a point X is located on Q_1 which is closest to MECI. The vector Q_2 then simply points from X to MECI. All the other points shown in Figures 7(d) and 7(f) (TS, paths and hopping geometries along the computed QM/MM trajectories) are then projected onto this 2D (Q_1,Q_2) plane. Based on the above table Tables S7 and S8 the vector Q_1 is simply $Twisted_{min}$ – $Planar_{min}$, and the vector Q_2 is MECI – X. Movies showing the trajectories on top of the 2D plane shown in Figures 7(d) and 7(f), and prototypical trajectories [including those selected in Figures 7(a–c)], are available in Supporting Information_2.

The use of gas-phase optimized structures is supported by evidence that they perfectly match the QM/MM optimized geometries in a solvent, as seen in Figure S25.

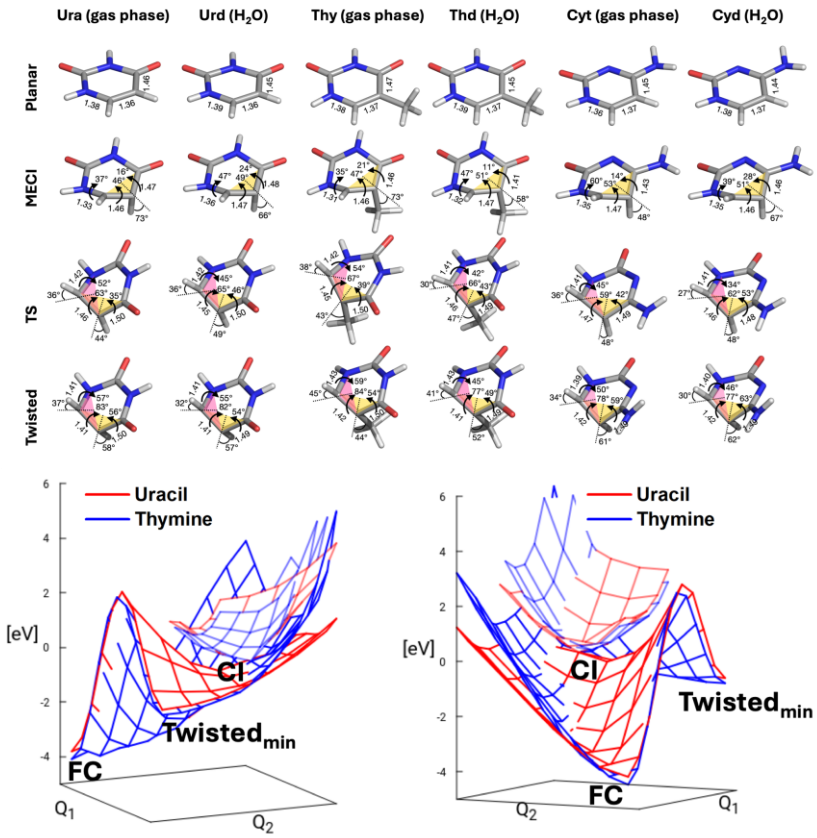

Figure S25. (top) Comparison between QM and QM/MM optimized geometries for planar, MECI, transition state and TI for pyrimidines in gas-phase and water-solvated pyrimidine nucleosides, with only QM region shown for clarity (top). Two orientations of excited state (S_1) and ground state (S_0) potential energy surfaces for Ura and Thy to indicate relative topological differences (bottom). The surfaces have been scaled along Q_1 and Q_2 to match the three critical points (FC ($Planar_{min}$), $Twisted_{min}$ and MECI) that define the (Q1,Q2) plane.

(e) Additional dynamical information

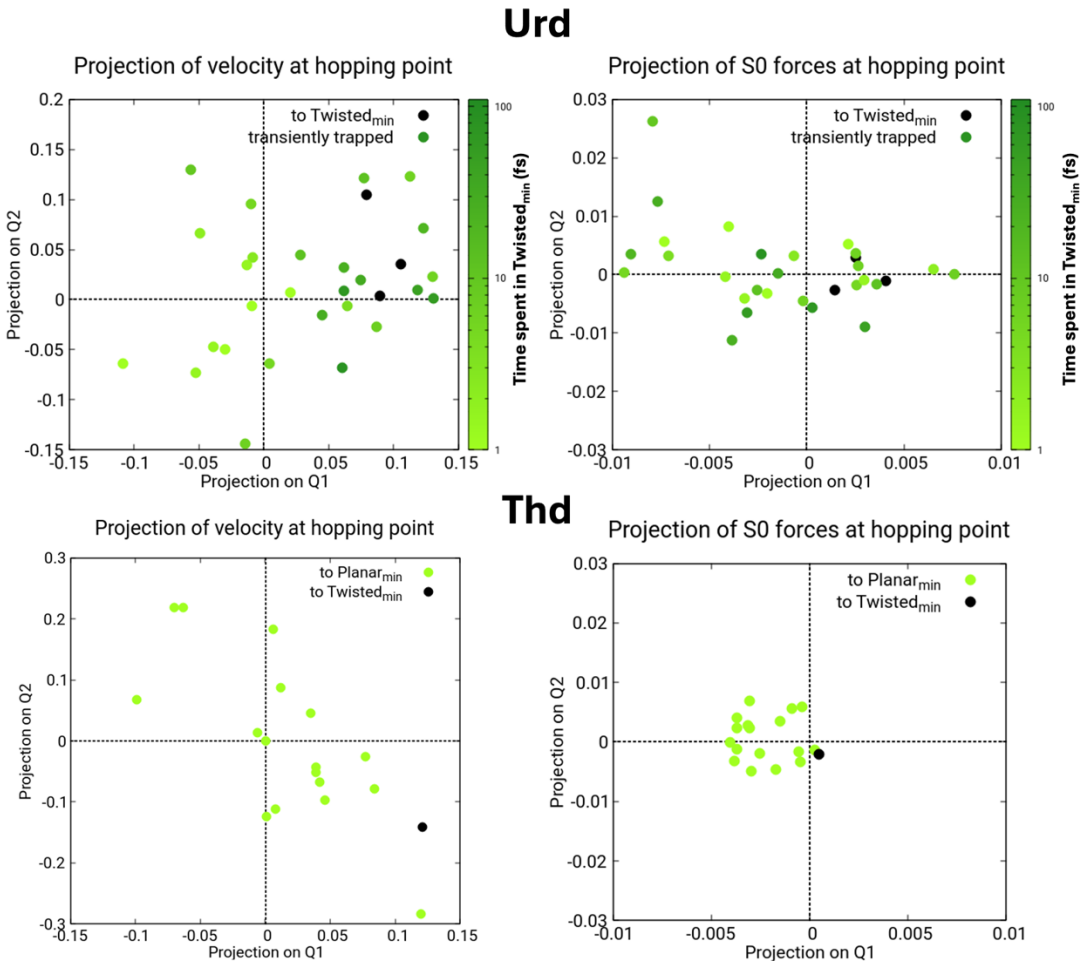

Figure S26. Projection of velocity (left) and ground-state (S_0) force (right) for hopping geometries shown in Figure 7 in main text (note that nonadiabatic nuclear dynamics leading only to one of two symmetry-equivalent TIs are displayed here; identical results hold also for other trajectories). Black dots correspond to trajectories that eventually form a stable TI, whereas green dots indicate trajectories that populate this region only transiently, with darker shading indicating increasingly longer lifetimes.

(f) QM/MM molecular dynamic simulations for Urd, Thd and Cyd

To determine the QY for TI formation following photoexcitation, we considered only those trajectories that decay to the ground state within the simulation time, comprising 43 trajectories for Urd, 44 for Thd and 41 for Cyd. In Figures S27–S29, trajectories that lead to TI formation are bordered in black, while those that are only transiently trapped in the twisted region are bordered in green.

Uridine

As shown in Figure S27, among 43 trajectories, eight (black-bordered panes) lead to TI formation (i.e., a TI that lives for at least 300 fs and is stable within the entire timescale of the dynamics), while six (green-bordered panes) are transiently trapped in the twisted region for ~20 to ~60 fs.

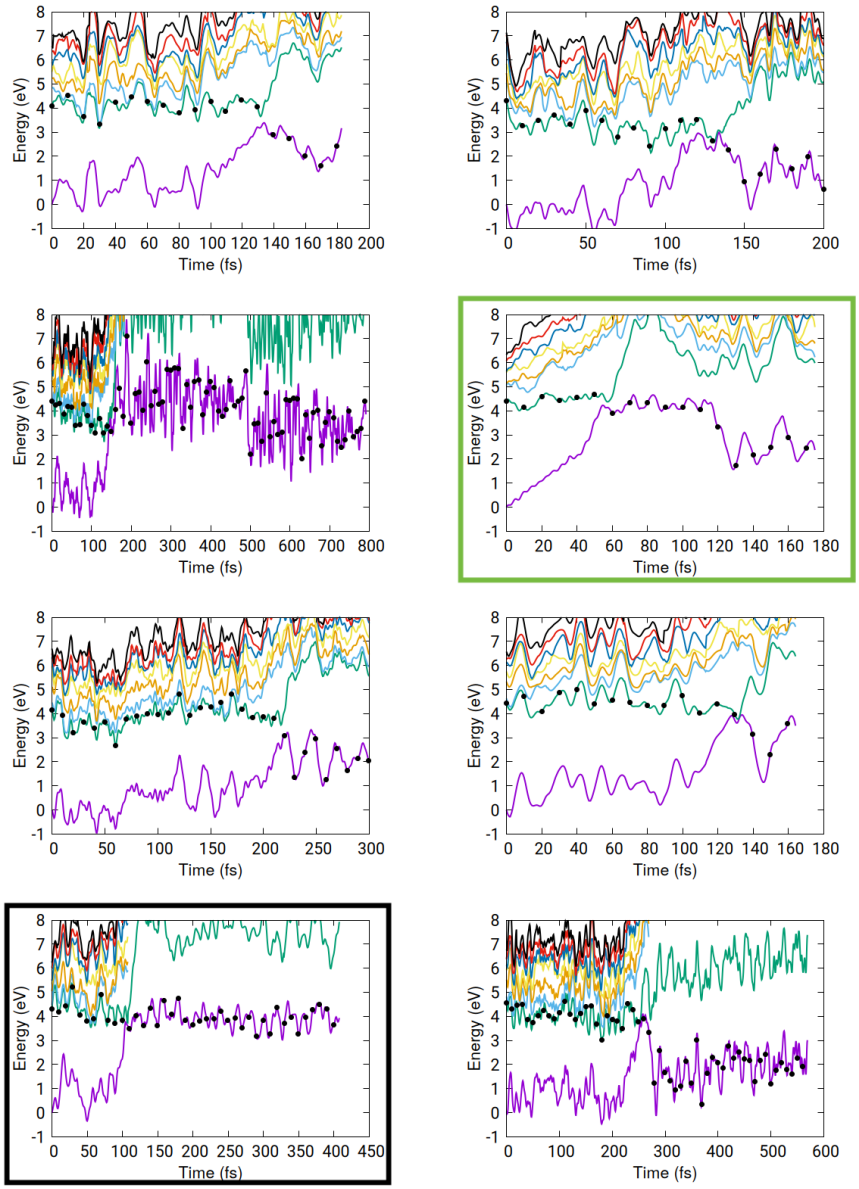

Figure S27. Trajectories obtained from QM/MM molecular dynamic simulations for Urd.

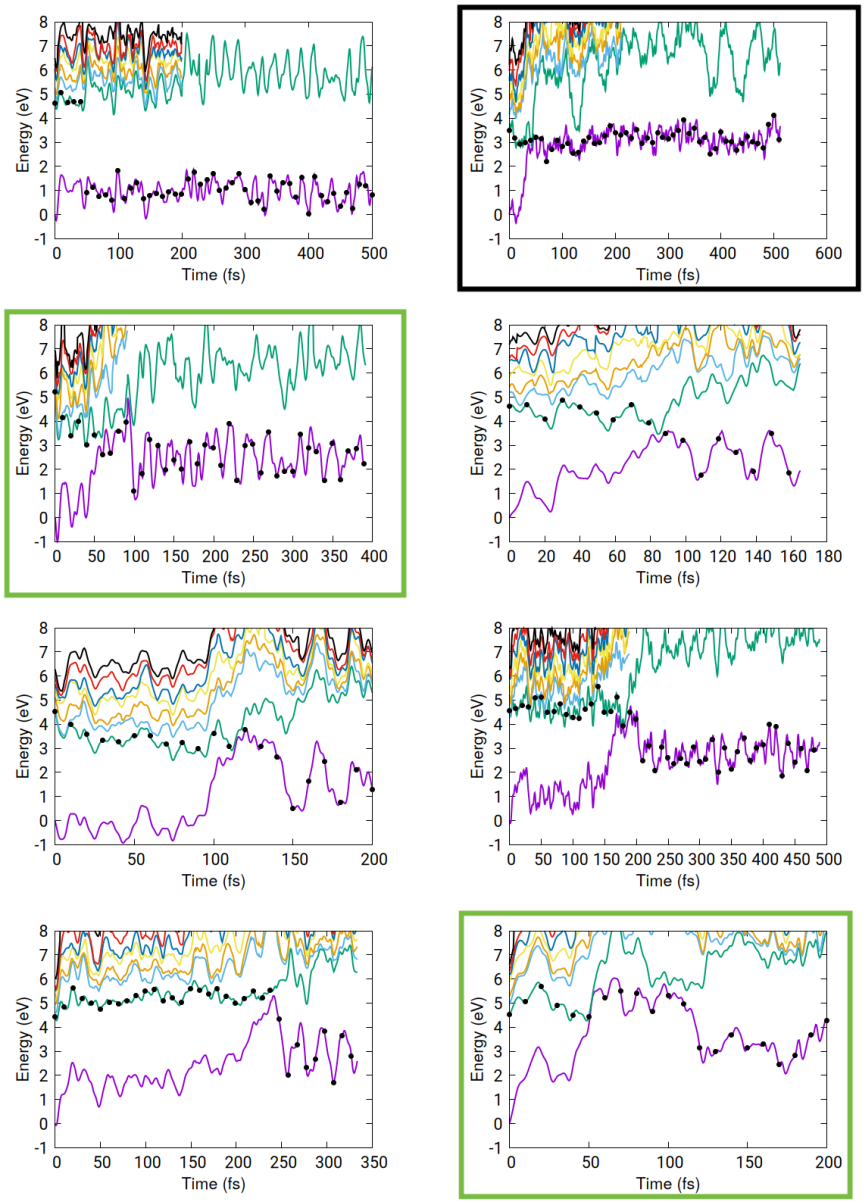

Figure S27 (Cont'd). Trajectories obtained from QM/MM molecular dynamic simulations for Urd.

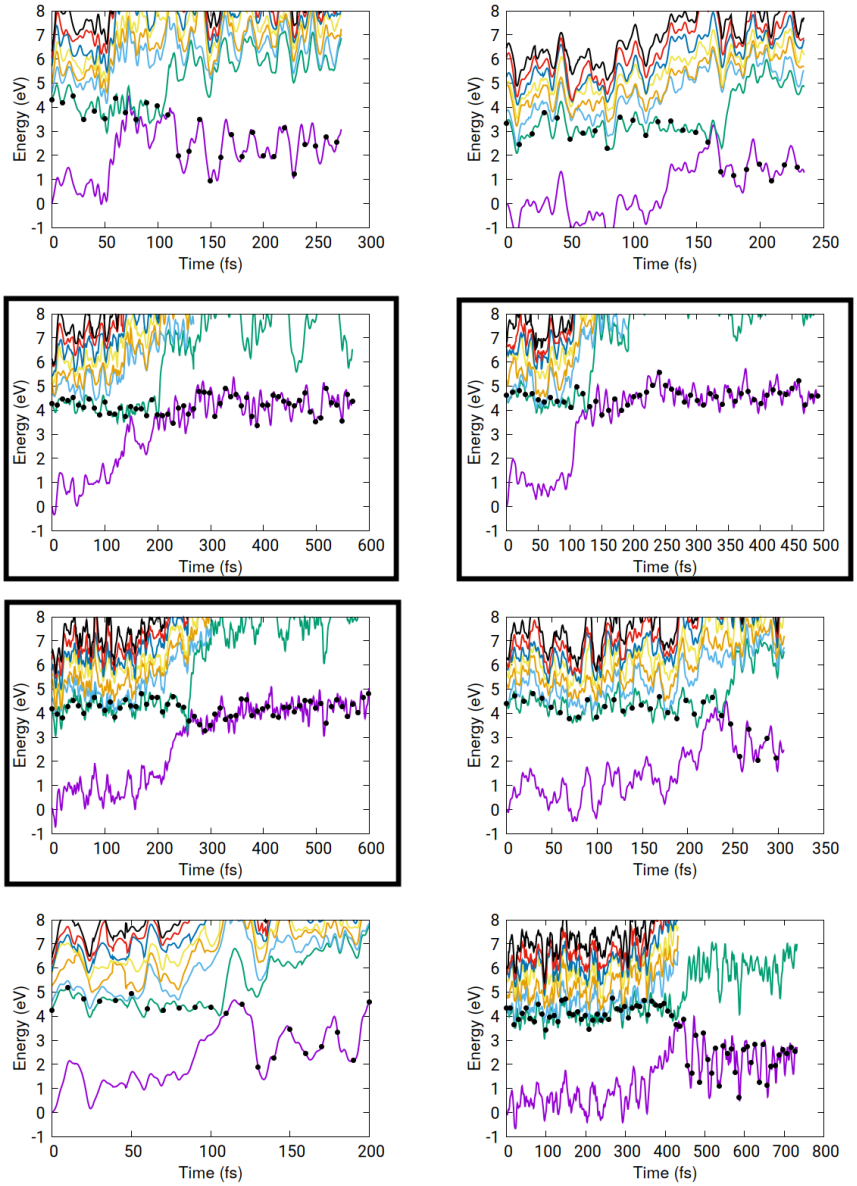

Figure S27 (Cont'd). Trajectories obtained from QM/MM molecular dynamic simulations for Urd.

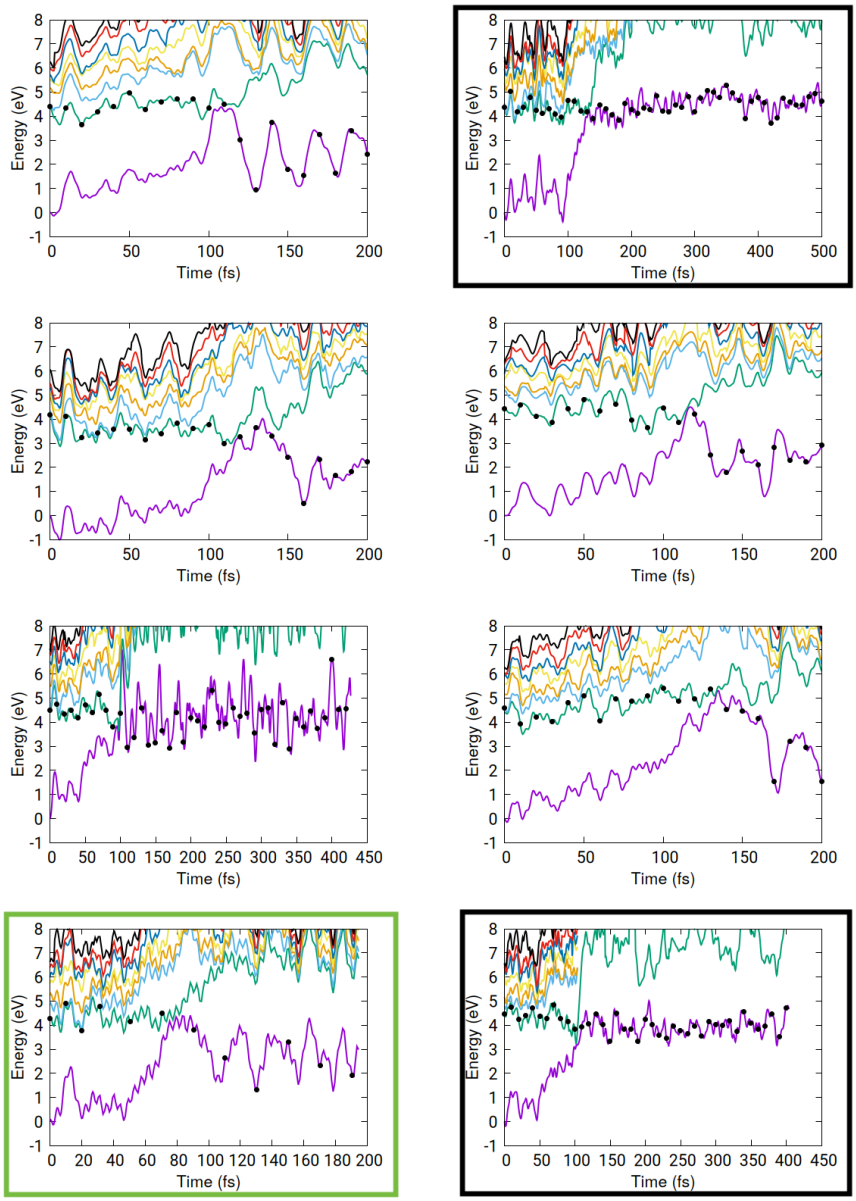

Figure S27 (Cont'd). Trajectories obtained from QM/MM molecular dynamic simulations for Urd.

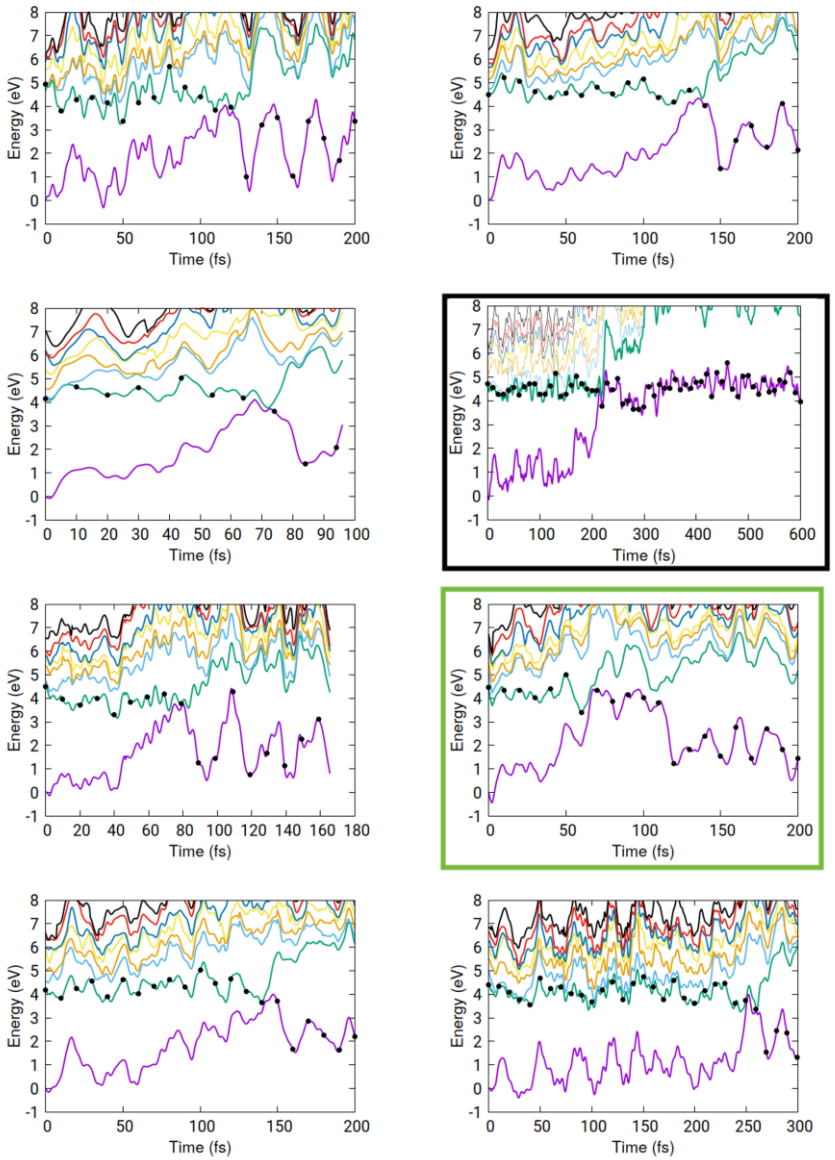

Figure S27 (Cont'd). Trajectories obtained from QM/MM molecular dynamic simulations for Urd.

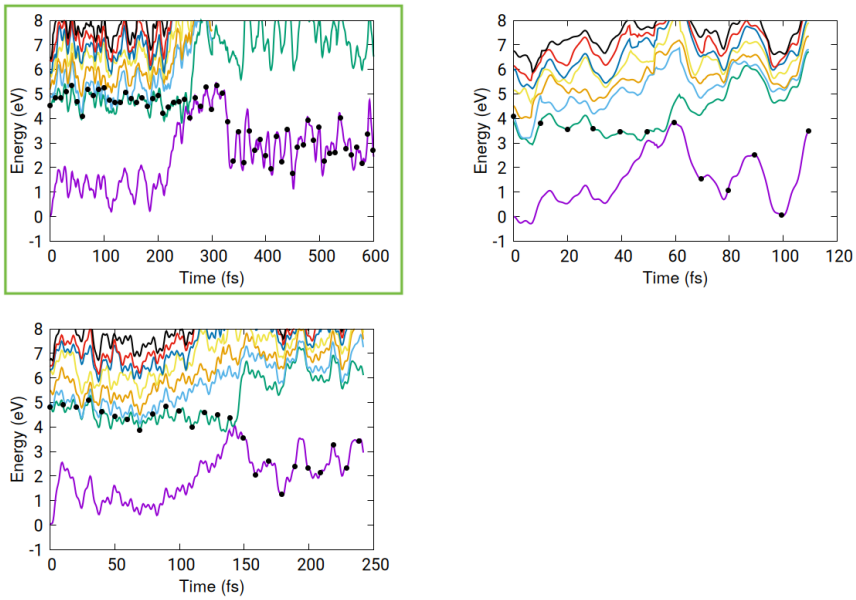

Figure S27 (Cont'd). Trajectories obtained from QM/MM molecular dynamic simulations for Urd.

Thymidine

As shown in Figure S28, among 44 trajectories, two (black-bordered panes) lead to TI formation (i.e., a TI that lives for at least 300 fs and is stable within the entire timescale of the dynamics), while two (green-bordered panes) are transiently trapped in the twisted region for ~80 fs and ~30 fs.

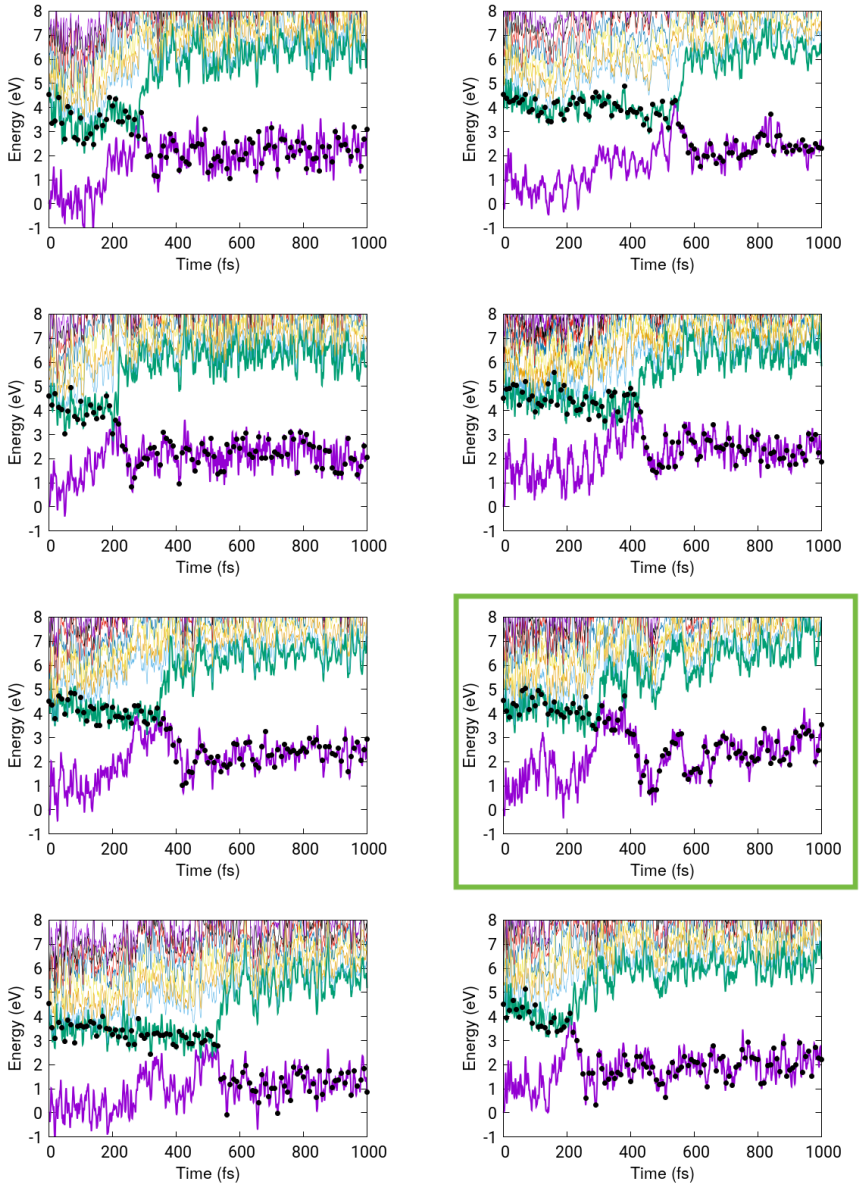

Figure S28. Trajectories obtained from QM/MM molecular dynamic simulations for Thd.

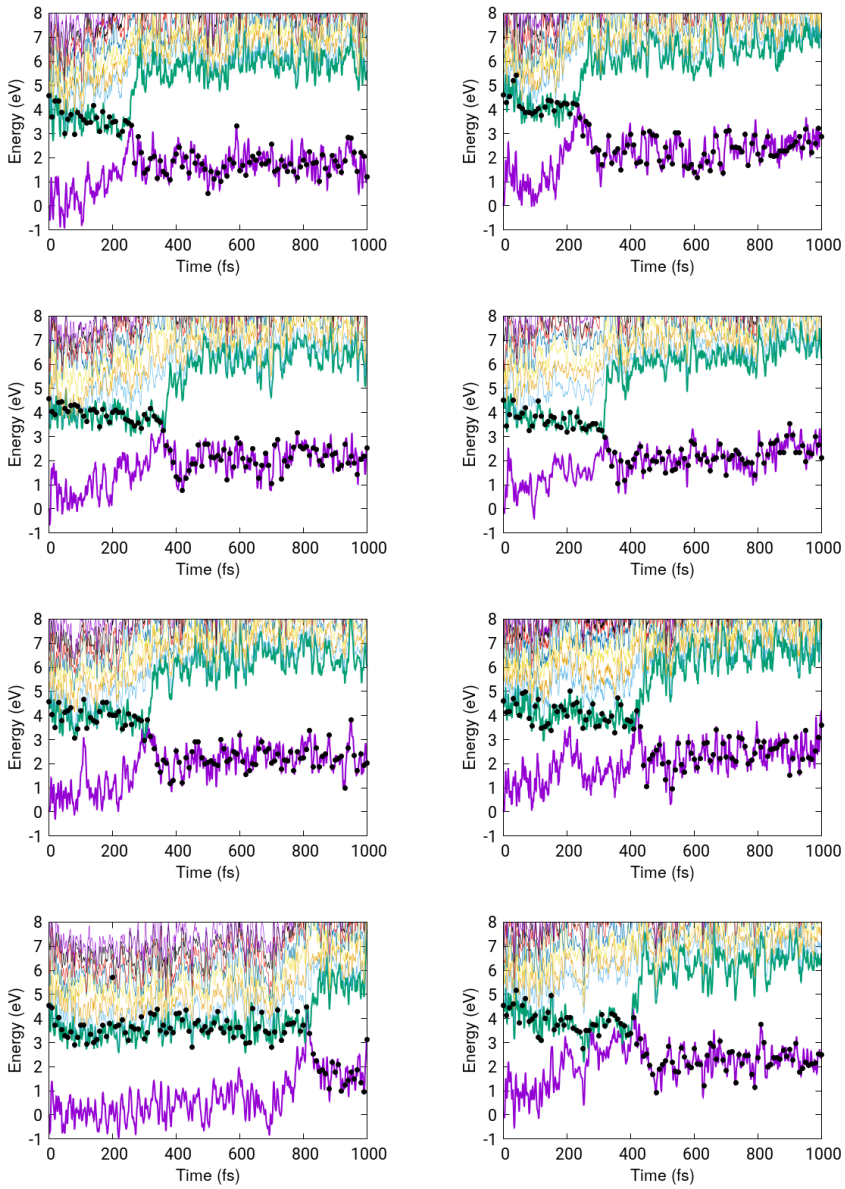

Figure S28 (Cont'd). Trajectories obtained from QM/MM molecular dynamic simulations for Thd.

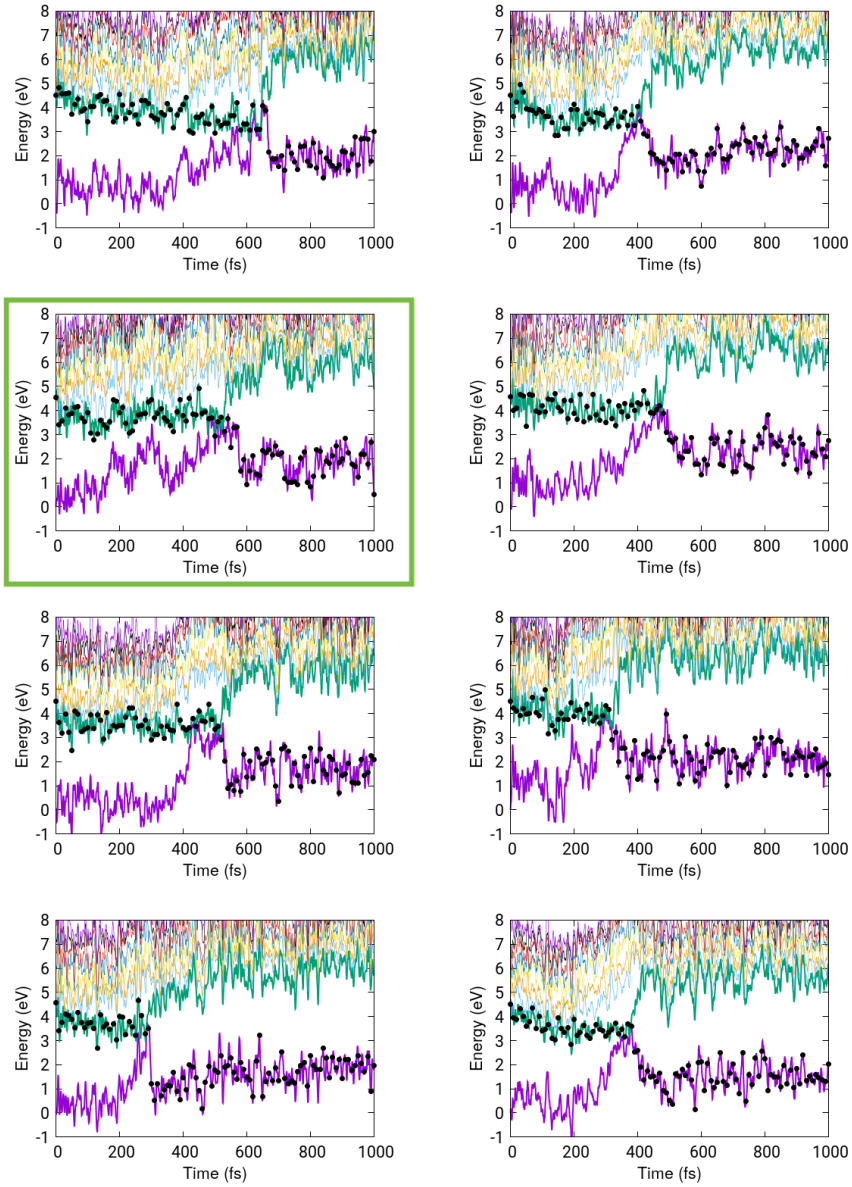

Figure S28 (Cont'd). Trajectories obtained from QM/MM molecular dynamic simulations for Thd.

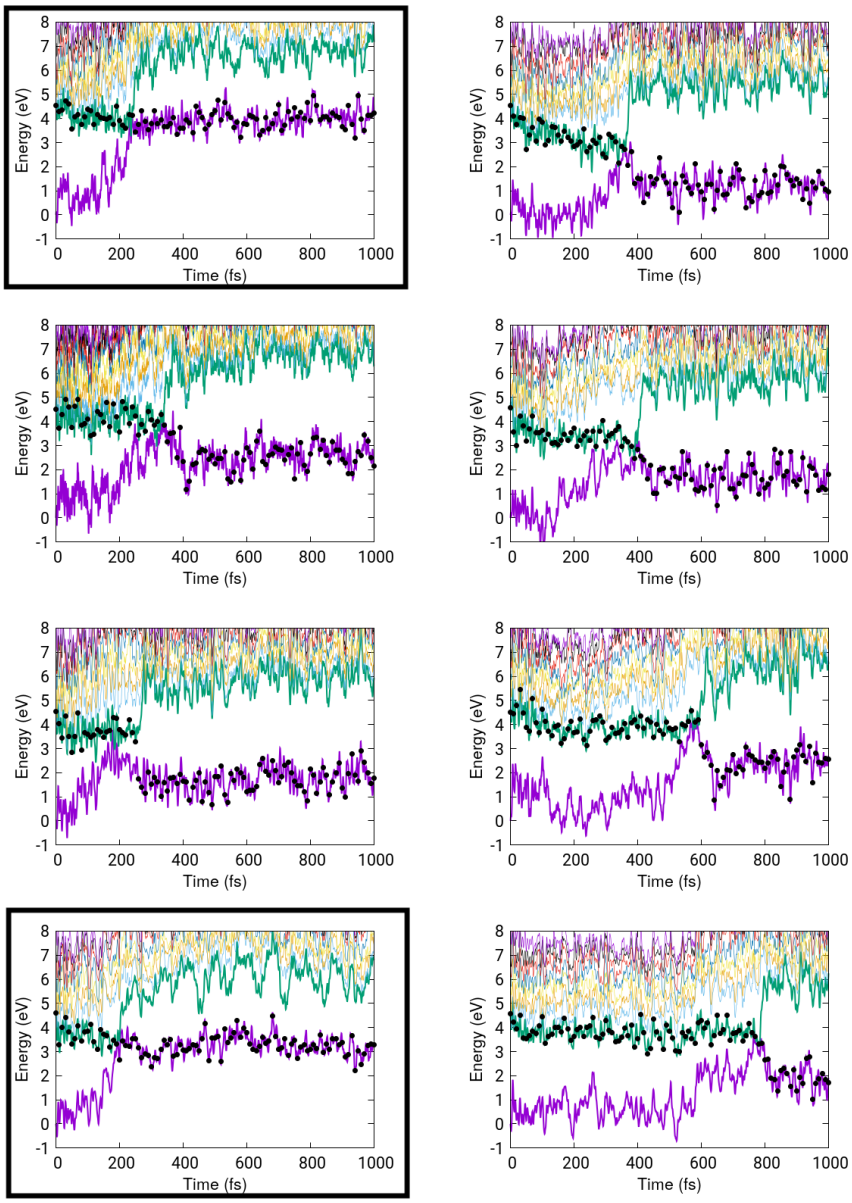

Figure S28 (Cont'd). Trajectories obtained from QM/MM molecular dynamic simulations for Thd.

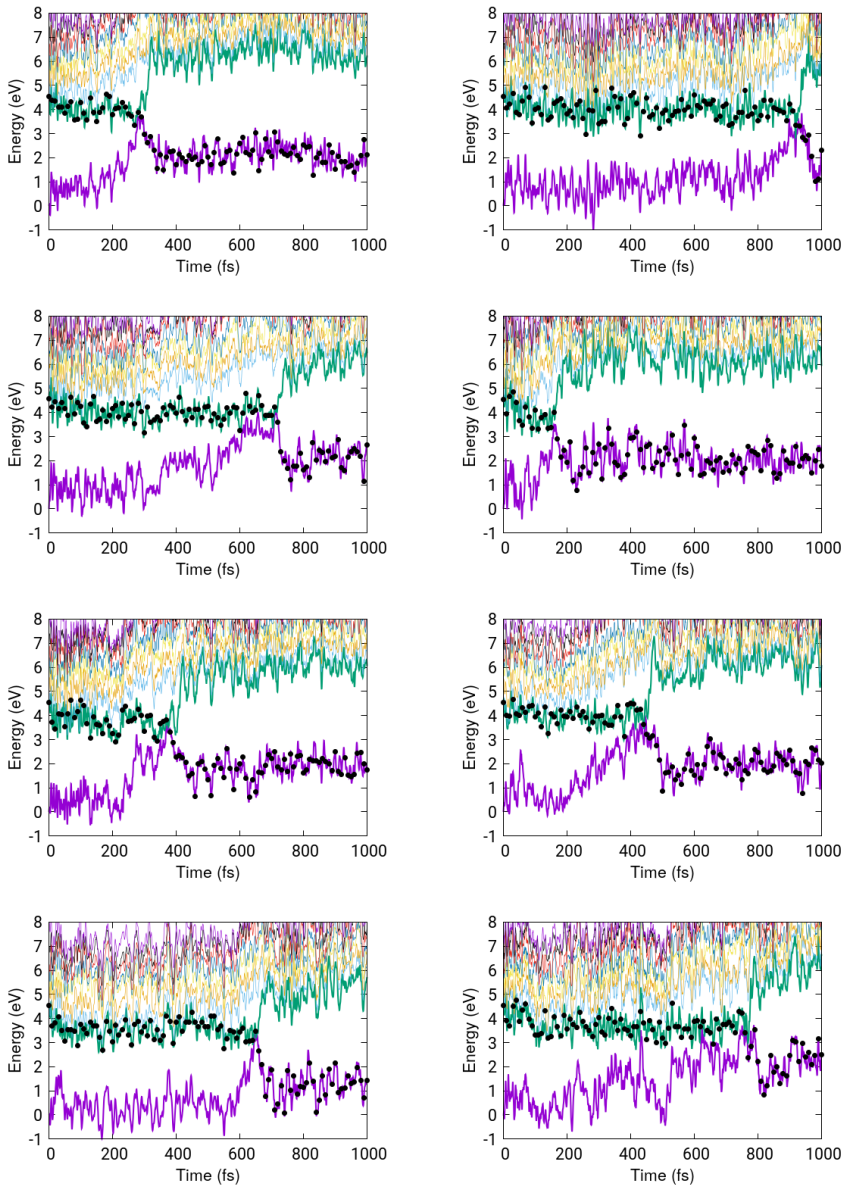

Figure S28 (Cont'd). Trajectories obtained from QM/MM molecular dynamic simulations for Thd.

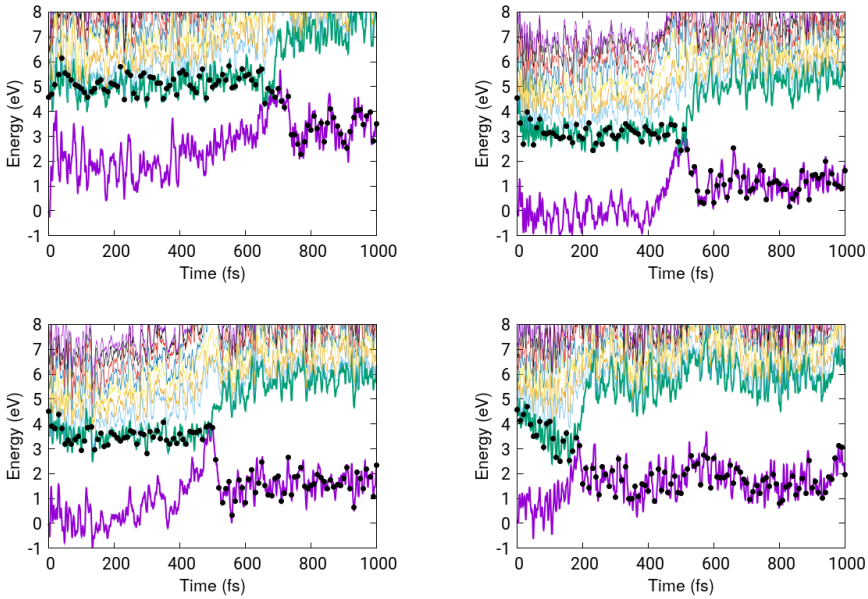

Figure S28 (Cont'd). Trajectories obtained from QM/MM molecular dynamic simulations for Thd.

Cytidine

As shown in Figure S29, among 41 trajectories, five (black-border panes) lead to TI formation (i.e., a TI that lives for at least 300 fs and is stable within the entire timescale of the dynamics), while three (green-bordered panes) are transiently trapped in the twisted region for ~40 to ~150 fs.

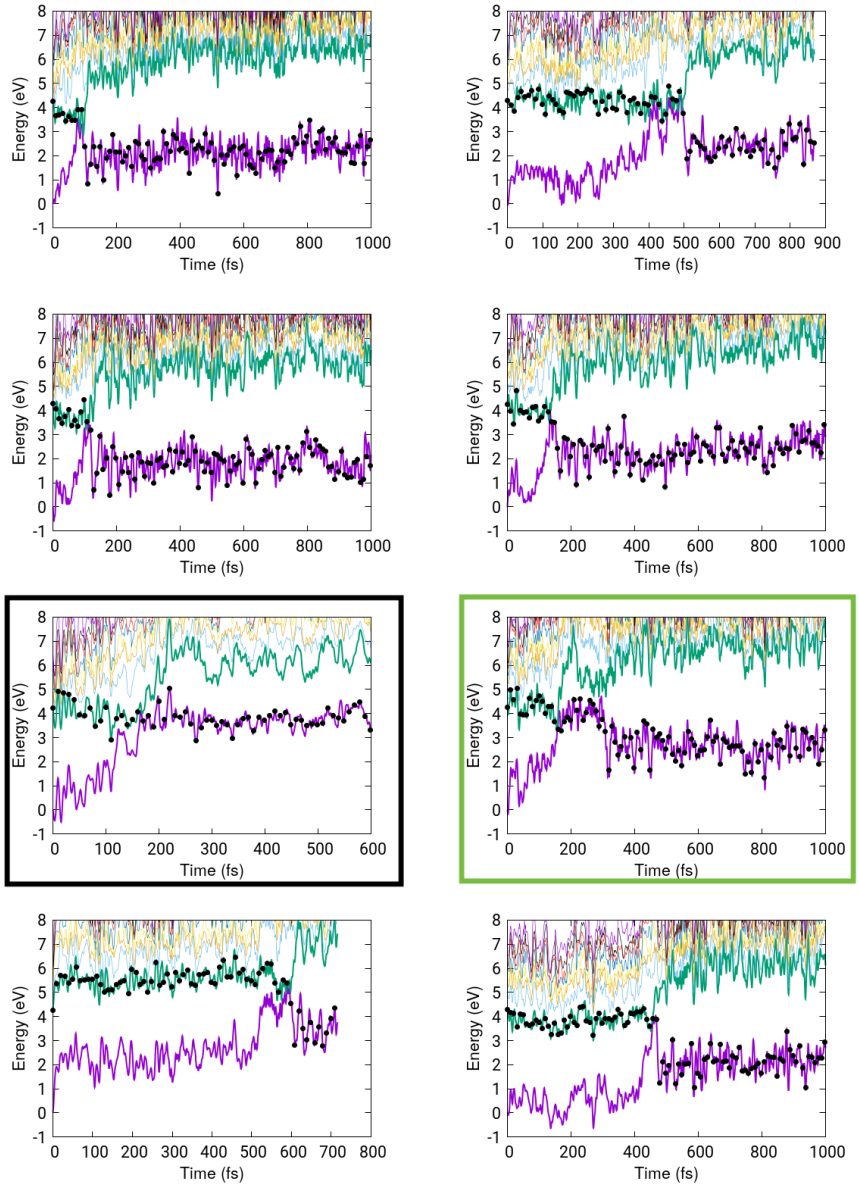

Figure S29. Trajectories obtained from QM/MM molecular dynamic simulations for Cyd.

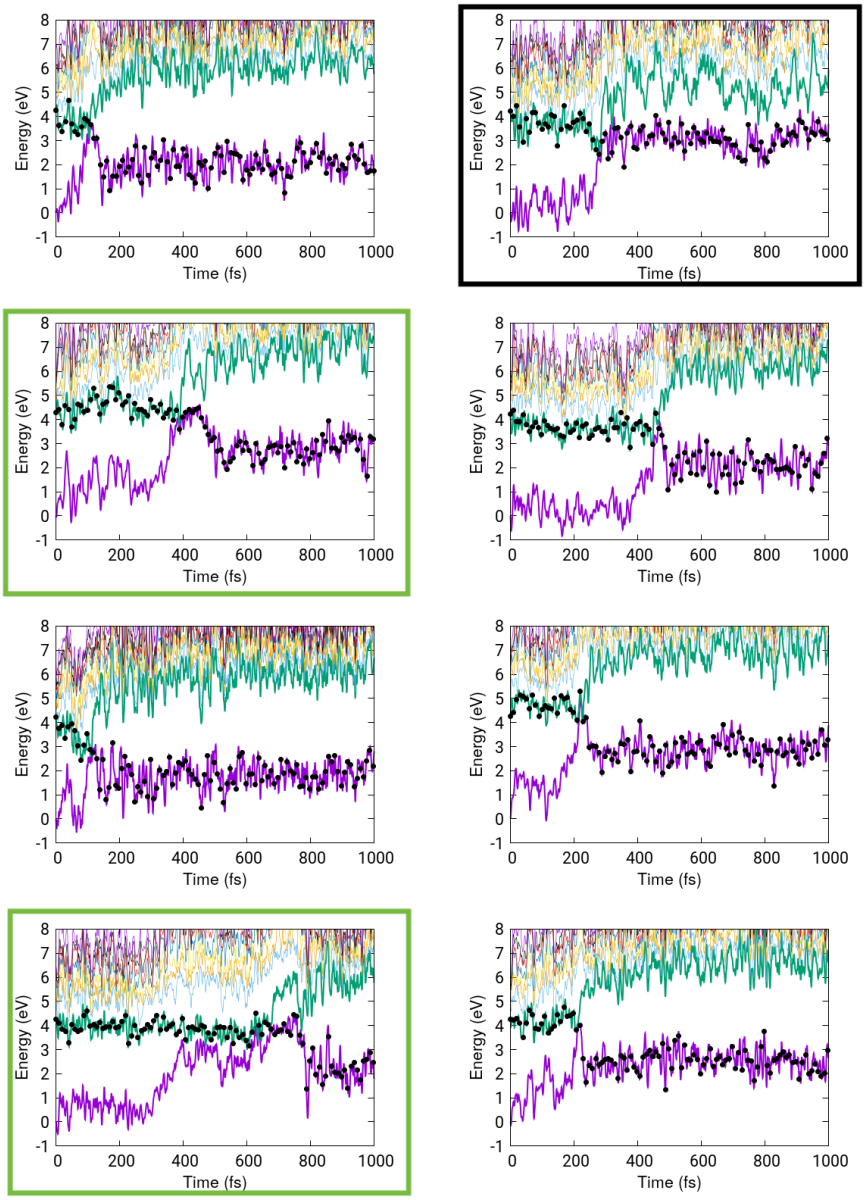

Figure S29 (Cont'd). Trajectories obtained from QM/MM molecular dynamic simulations for Cyd.

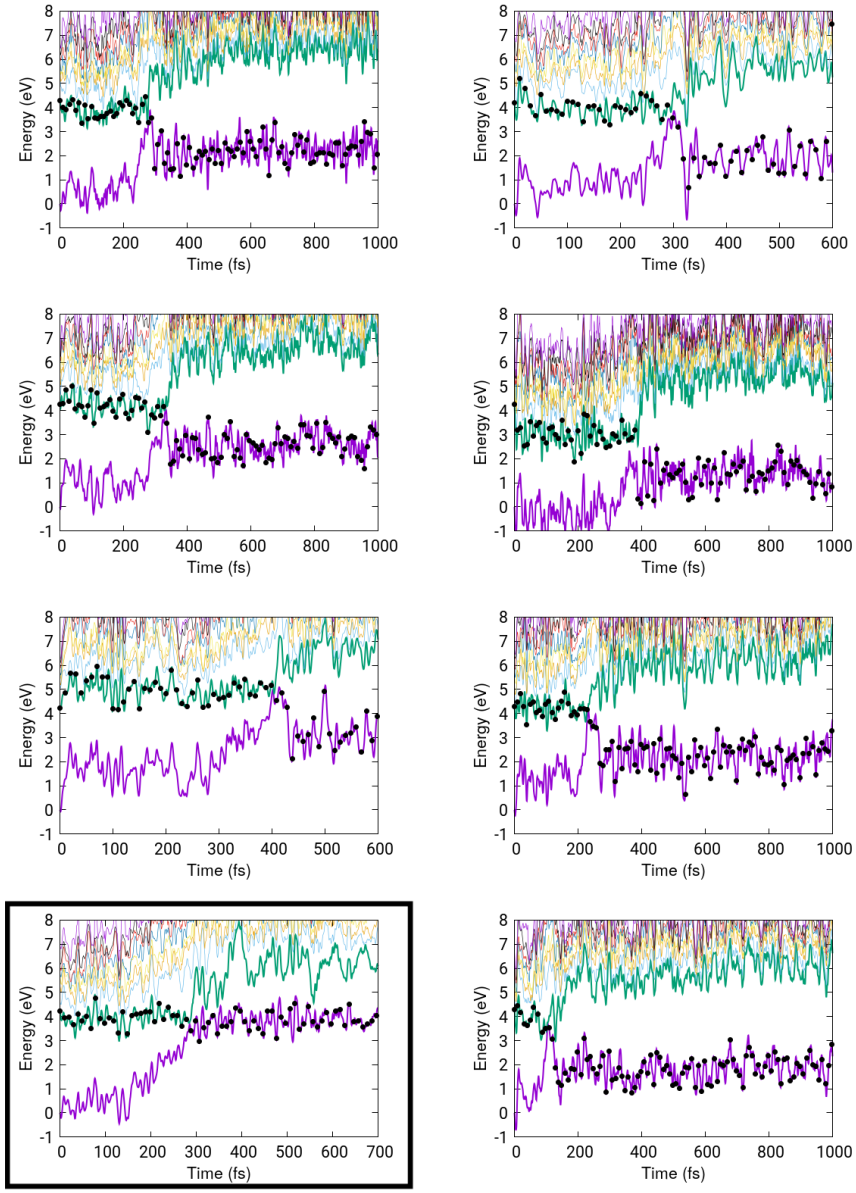

Figure S29 (Cont'd). Trajectories obtained from QM/MM molecular dynamic simulations for Cyd.

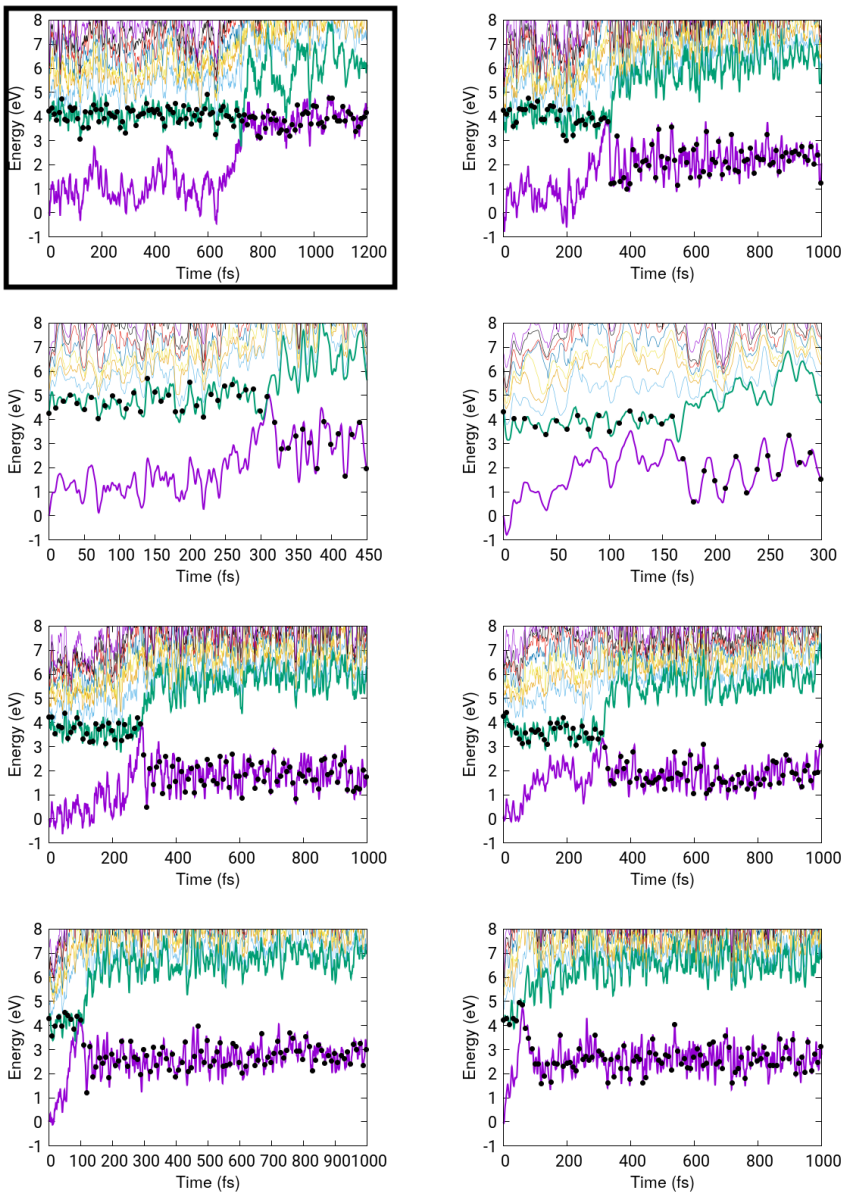

Figure S29 (Cont'd). Trajectories obtained from QM/MM molecular dynamic simulations for Cyd.

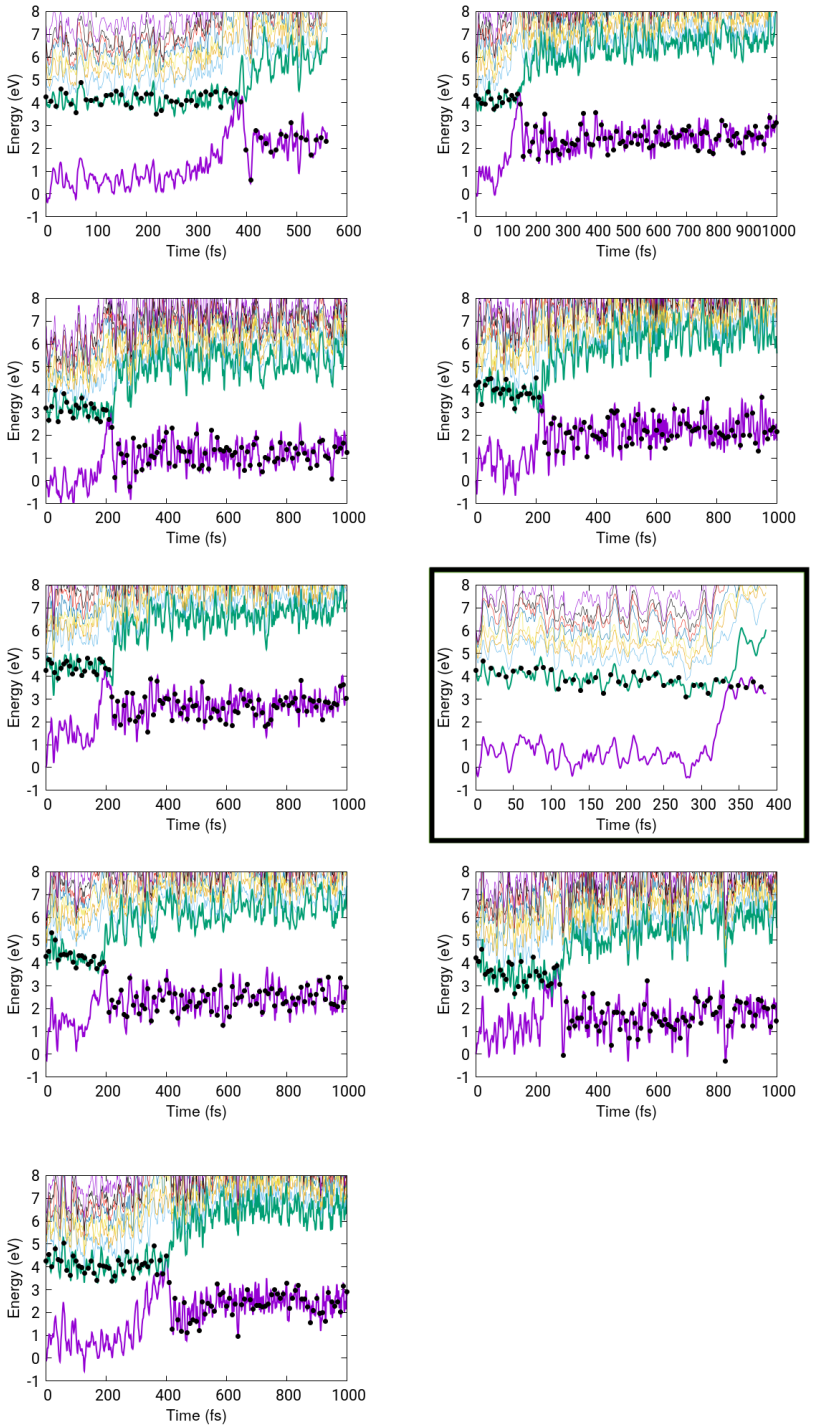

Figure S29 (Cont'd). Trajectories obtained from QM/MM molecular dynamic simulations for Cyd.

(g) Frontier natural orbitals of twisted intermediate for solvated Urd

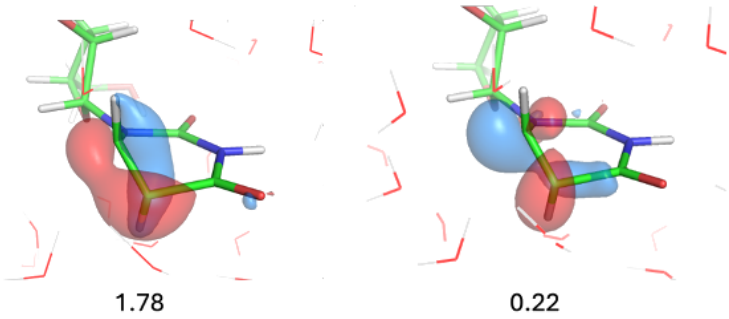

Figure S30. Frontier natural orbitals and occupation numbers for Urd in water computed at RMS-CASPT2/SA-2-CASSCF(6,6) level of theory.

H. Calculation of charges on C5 and C6

In the 1960-1970s, it was shown that the hydration reaction proceeds with preferential insertion of an OH group at the C6 carbon. Some researchers therefore proposed this to be the result of polarization of the C5=C6 double bond, where C6 carries a partial positive charge.[3] Our results are consistent with this interpretation, although earlier studies were based on a planar structure. To examine this point, we compared the partial charges on the C5 and C6 carbon atoms for the planar and twisted ground states of Ura and Cyt derivatives; the results are summarized in Figure S31 and Table S9. These values were calculated using natural population analysis (Pop=NPA keyword in Gaussian 16) at the B3LYP/def2-TZVP+PCM(H_2O) level of theory. For nonmethylated derivatives, the bond polarity is slightly enhanced in the TI. In contrast, the polarity decreases for C5 substituted derivatives. Thus, twisting enhances the difference in reactivity between compounds with H or methyl at the C5 position.

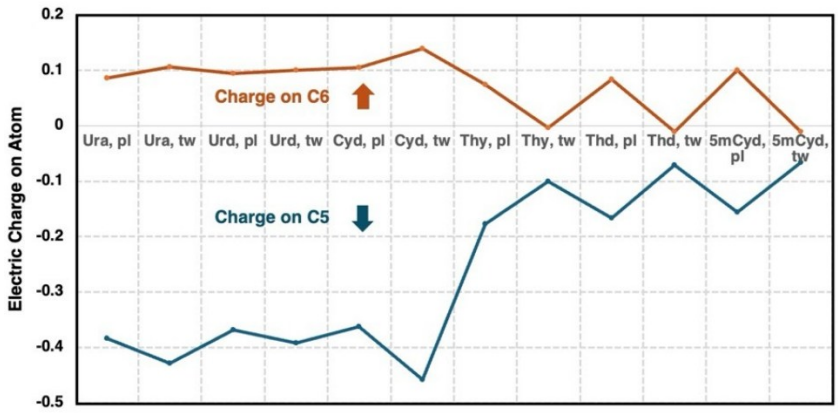

Figure S31. Charges on C5 and C6 for different nucleobases and their derivatives obtained from NPA analysis using B3LYP/def2-TZVP+PCM(H_2O) level of theory.

Table S9. Partial charges on C5 and C6 estimated using NPA at B3LYP/def2-TZVP+PCM(H_2O) level of theory

Molecule, geometry	**C5**	**C6**
Ura, planar	-0.384	0.086
Ura, twisted	-0.429	0.106
Thy, planar	-0.177	0.075
Thy, twisted	-0.100	-0.003
Urd, planar	-0.368	0.095
Urd, twisted	-0.392	0.100
Thd, planar	-0.166	0.084
Thd, twisted	-0.071	-0.011
Cyd, planar	-0.362	0.105
Cyd, twisted	-0.458	0.140
5-methylCyd, planar	-0.156	0.101
5-methylCyd, twisted	-0.066	-0.010

References

1. Malone, R. J.; Miller, A. M.; Kohler, B., Singlet Excited-state Lifetimes of Cytosine Derivatives Measured by Femtosecond Transient Absorption. *Photochem. Photobiol.* **2003,** *77* (2), 158-164.
2. Obara, Y.; Ghosh, S.; Kamibashira, S.; Suzuki, T., Solvent Effects on the Formation of Ground-State Twisted Intermediate during Electronic Relaxation of Pyrimidine Nucleobases. *J. Am. Chem. Soc.* **2025,** *147* (45), 41284-41296.
3. Fisher, G. J.; Johns, H. E., 4 - Pyrimidine Photohydrates. In *Photochemistry and Photobiology of Nucleic Acids*, Wang, S. Y., Ed. Academic Press: 1976; pp 169-224.